

A Mathematical Procedure for Solving the Inverse Potential Problem of Electrocardiography. Analysis of the Time-Space Accuracy from In Vitro Experimental Data*

P. COLLI-FRANZONE AND L. GUERRI

*Dipartimento di Informatica e Sistemistica, Università di Pavia,
and Istituto di Analisi Numerica del CNR, Pavia, Italy*

S. TENTONI AND C. VIGANOTTI

Istituto di Analisi Numerica del CNR, Pavia, Italy

AND

S. BARUFFI, S. SPAGGIARI, AND B. TACCARDI

Istituto di Fisiologia Generale, Università di Parma, Italy

Received 18 December 1984; revised 18 December 1984

ABSTRACT

The inverse potential problem of electrocardiography leads to a Cauchy problem for an elliptic operator and is strongly ill posed. Its solution must be determined by some regularization technique in which a parameter controls the amount of regularization of the solution. Therefore the choice of this smoothing parameter is important for achieving the best accuracy attainable given the discrete approximation errors and the noise level on the data. A regularized inverse procedure is applied to data from an in vitro experiment, and a new criterion for the choice of a quasi-optimal value of the smoothing parameter is described. The performance of this criterion is investigated, and a detailed analysis of the accuracy of the results is carried out. This analysis concerns both the recovered epicardial maps (space analysis) and the ECGs (time analysis).

INTRODUCTION

The computation of body surface potential distributions from epicardial potentials and conversely the determination of epicardial potential distributions from body surface potentials constitute respectively the direct and inverse potential problems of electrocardiography.

*This work was supported through grants by MPI 40%, the Special Program on Bioengineering of CNR and IAN of CNR.

Recent attempts to solve the inverse potential problems by using data from in vitro [7, 8, 10, 11] and in vivo [20, 3] dog experiments have shown that qualitatively reliable estimates of the epicardial potential distributions can be obtained from surface potential data. These estimates are of physiological interest in that they yield information about the underlying intracardiac events which can be inferred only partially by inspecting the corresponding surface potential distributions. However, it must be pointed out that the quality level of the recovered potential patterns available in the literature is not uniform over the entire heart beat. The computed potentials are affected by considerable quantitative errors, with an average relative error of about 0.6 for data collected in vitro [7, 8, 10, 11] and 0.8 for in vivo [20, 3].

In view of these discrepancies, the interpretation of the computed epicardial distributions is often difficult. In the in vivo experiments these quantitative errors can be attributed to several causes beside the noise affecting the data and the model discretization errors, namely:

- (1) the disregard of body inhomogeneities in order to make the problem more amenable to numerical treatment;
- (2) the reconstruction of the epicardial potential on a fixed surface, whereas the measured data were recorded from the moving surface of the beating heart;
- (3) the choice of a smoothing parameter, in the inverse method, which was constant throughout the heart beat, so that the accuracy of the computed epicardial potential was not the best possible.

To our knowledge an assessment of the influence of these error sources on the accuracy of the epicardial potential estimates is not yet available (see e.g. [17]). Thus there are no clear guidelines for the improvement of the computed epicardial potential maps (CEPMs).

The results previously published by our group [7, 8, 10, 11] concern an in vitro experiment with a cylindrical homogeneous conducting medium [25, 26]. The epicardial data were measured, and the CEPMs were estimated on a fixed surface surrounding the heart. Since the heart was placed in a central position in a tank, it was everywhere fairly distant from the outer surface, so that the inverse problem was more ill conditioned than in human subjects, where the heart is close to the anterior side of the thorax. This proximity may be a favorable factor for the solution of the inverse problem, since a higher accuracy can be expected in the anterior epicardial patterns, which convey a large amount of information.

In order to investigate how far the accuracy of the CEPM could be improved in a more realistic geometry, a new experiment in vitro was planned where an isolated dog heart was placed inside a tank shaped like a child torso, close to the normal heart location.

In this paper we shall carry out a detailed analysis of the accuracy of the epicardial estimates obtained by using data from the above experiment, so that the only possible factors affecting the accuracy were the noise on the thoracic and epicardial potential measurements, slight errors in the measurements of the electrode coordinates, and the model discretization errors.

The salient points in our approach are:

(1) the transfer matrix linking epicardial to body surface potential was obtained by the finite-element method (FEM), where the volume conductor was approximated by a three-dimensional (3-D) mesh with surface grids finer than those previously used for *in vitro* or *in vivo* experiments;

(2) the inverse procedure was first applied by using those values of the smoothing parameter that optimized the accuracy of the CEPMs with respect to the measured epicardial potential distributions;

(3) subsequently we investigated the efficiency of a criterion (CRESO) for choosing a time-dependent smoothing parameter that does not require a prior knowledge of either the epicardial data or the characteristics of the noise affecting the thorax data;

(4) we applied the inverse procedure to the entire normal heart beat including the *P* wave, and we evaluated the accuracy of the computed results in terms of the instantaneous potential distributions (maps) and also in terms of the reconstructed electrocardiograms (ECGs);

(5) finally, in solving the direct and inverse problems, the transfer matrix and the computed epicardial and chest potentials were not adjusted by taking into account the measured data [20, 6].

EXPERIMENTAL PROCEDURE

In every experiment two mongrel dogs of different size (average weight 15 and 25 kg) were anesthetized with Na-penobarbital (30 mg/kg). The heart of the smaller dog was isolated and Langendorff-perfused with blood from the carotid artery of the other dog (donor dog). The blood from the pulmonary artery of the isolated heart was returned to the donor dog through the external jugular vein.

The isolated heart was placed in a cage (or frame) made of nylon wires and Perspex rings (Figure 1). The cage supported 216 electrodes regularly distributed with an angular increment of 15° along 9 horizontal circumferences, spaced 1 cm vertically. The radii of the circumferences ranged between 2.5 and 5 cm. The centers of all the circumferences lay on the same vertical axis (rotation axis). The electrodes were made of 0.1-mm silver wire, insulated except for the last millimeter. The cage with the isolated heart was immersed in a tank molded on the torso of a nine-year old child (Figure 1).

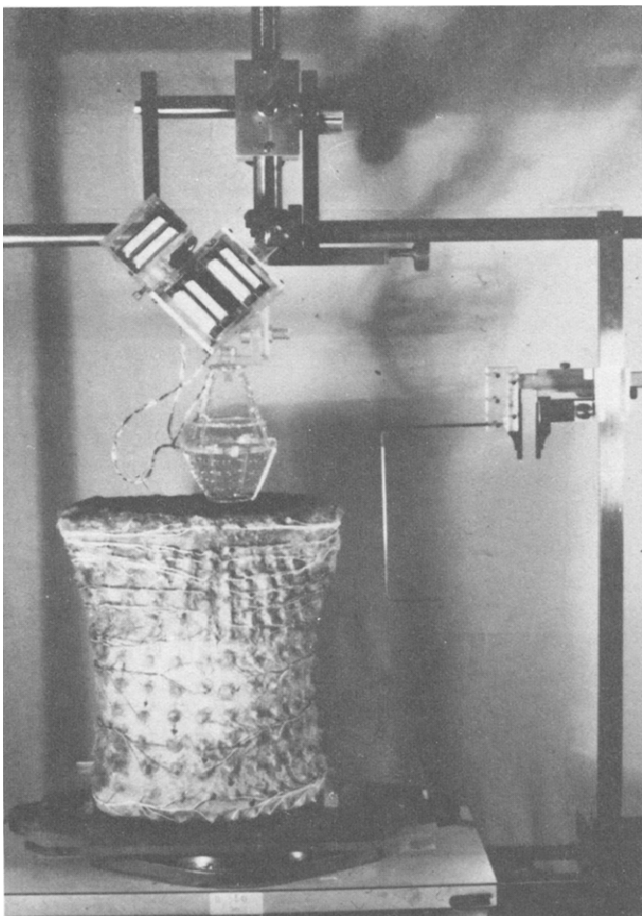


FIG. 1. A view of the thorax-shaped tank and of the epicardial cage used in the experiment.

The cage, which will be referred to as the *epicardial* frame, was placed in a position similar to that occupied by the heart in a human chest (Figure 2). The epicardial surface of the isolated heart was at an average distance of 1 cm from the cage.

The tank was 33 cm high. The transverse and anteroposterior diameters were about 25 cm and 14 cm. The tank was filled with a modified Ringer solution containing (mM/l) NaCl 157, KCl 5.6. CaCl₂ was not added to prevent clotting of the small amount of blood that leaked from the (heparinized) heart. The resistivity of the solution was about 50 Ω cm.

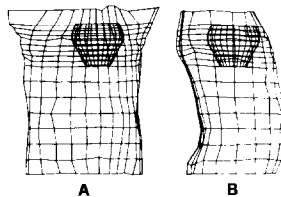


FIG. 2. Orthogonal projections of the quadrilateral mesh approximating the thorax-shaped tank surface and the epicardial cage: (a) anterior projection; (b) lateral right projection.

Four hundred spherical silver electrodes (2 mm in diameter) were fixed to the inside of the thorax on 17 horizontal contours spaced vertically 1 cm at the level of the cage, 3 cm elsewhere. The electrodes were spaced with an angular step of 15° along each horizontal contour by taking the axis of symmetry of the internal cage as the rotation axis.

Unipolar electrocardiograms (ECGs) were recorded, 200 at a time, from all the electrodes on the chest and on the cage. Every ECG was the expression of the potential difference between one of these electrodes and a common reference electrode placed at a great distance from the heart, at the bottom of the tank. Three electrodes on the cage were used to record three reference ECGs together with each group of 200 ECGs. These reference ECGs were used for the time alignment of the successive groups of recordings by means of cross-correlation. The reference tracings were also used to make sure that the electrical activity of the heart remained stable during the entire exploration.

The 203 signals were simultaneously amplified and converted to digital form (8 bits) at a sampling rate of 500 Hz per channel [12], conveyed to a PDP11/40 minicomputer, and stored on tape. The coded data were converted to microvolt values, and the time skew introduced by the sequential sampling, amounting to 2 msec from the first to the last sample in a switch cycle, was compensated for by means of linear interpolation.

The 616 waveforms (400 from the thorax and 216 from the cage) were displayed graphically by means of a Calcomp plotter, and a quality control was performed.

The overall noise on the measured potential maps was compounded by:

(1) *Noise due to the electronic instrumentation*, i.e. amplifiers and analog-to-digital conversion (A.D.), with an estimated standard deviation (S.D.) of 5–6 μV for signals of amplitude lower than 300 μV , which were linearly converted. For higher signals the A.D. conversion was logarithmic, and therefore an error of about ± 2 percent of the signal value added itself to the amplifier noise, whose S.D. was of 4–5 μV .

(2) *Errors introduced by the time-alignment of the signals.* This error could overwhelm the instrumental noise in those time intervals where the potential underwent rapid changes.

MATHEMATICAL PROCEDURES

Let Γ_1 be the tank surface shaped like a child thorax (closed at the shoulders, neck, and bottom), Γ_0 the closed surface spanned by the epicardial frame surrounding the isolated heart, and Ω the volume bounded by Γ_0 and Γ_1 .

By means of the electrodes located on Γ_0 and Γ_1 , plus some interpolated points, it is possible to define a mesh made up of quadrilateral elements on the surfaces (Figure 2). Moreover, these meshes can be connected by means of a 3-D mesh composed of hexahedral elements and approximating the domain Ω . This 3-D mesh is obtained by suitably connecting the vertices of the net on each horizontal section (Figure 3).

To simplify the notation, we shall use the same symbols Γ_0, Γ_1 to denote the original surfaces and their approximation by means of the quadrilateral elements defined by the nodes of the surface meshes; the same holds for Ω and its approximation by means of hexahedral elements.

Assuming that the cardiac electric field is quasistatic [1, 18, 19] and that Ω is an isotropic and homogeneous volume conductor, the electric cardiac potential $V(x, t)$ is the solution of the problem:

$$\begin{aligned} \Delta V(x, t) &= 0 && \text{in } \Omega, \\ V(x, t) &= u(x, t) && \text{on } \Gamma_0, \\ \frac{\partial V(x, t)}{\partial n} &= 0 && \text{on } \Gamma_1, \end{aligned} \quad (1)$$

where $u(x, t)$ is the epicardial potential distribution at time t , $\Delta = \sum_{i=1,3} \partial^2 / \partial x_i^2$, and n is the unit vector normal to Γ_1 . The condition $\partial V / \partial n = 0$ on Γ_1 is related to the fact that the tank is made of an insulating

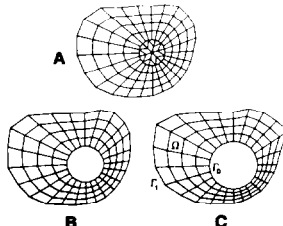


FIG. 3. Examples of horizontal mesh sections of the 3-D mesh approximating the volume conductor Ω : (a) mesh section not intersecting the cavity Γ_0 ; (b),(c) mesh sections intersecting Γ_0 at different heights from its lower basis.

material and the solution surface of the conducting medium is in contact with the air; therefore on Γ_1 the normal component of the electric field is zero.

The trace of V on Γ_1 is the thorax potential distribution. Denoting this trace by $z(x, t)$, the problem (1) defines a linear operator A , independent of t , which transforms $u(x, t)$ into $z(x, t)$.

The *direct problem of electrocardiography*, in terms of potential alone, consists in finding $z(x, t)$ from the knowledge of $u(x, t)$, i.e. solving the problem (1).

If this problem is discretized by means of the finite-element method (FEM) [8, 22, 32] applied to the variational formulation of (1), i.e.,

find $V(x, t)$ such that $V|_{\Gamma_0} = u$, $\int_{\Omega} \nabla V(x, t) \cdot \nabla \phi(x) dx = 0$, for any regular $\phi(x)$ on Ω with $\phi|_{\Gamma_0} = 0$,

then the transfer operator A is approximated by a transfer matrix T of dimensions $n_1 \times n_0$, where n_1, n_0 are the numbers of nodes respectively on Γ_1 and Γ_0 .

We shall denote by $\mathbf{u}(x, t)$ the values of $u(x, t)$ at the grid nodes on Γ_0 . For t fixed we have the nodal values at that time, i.e. a surface map; for x fixed we have the time sequence of potential values at x , i.e. an ECG. We shall use the notation $\mathbf{u}(t)$ and $\mathbf{u}(x)$ to indicate that we keep t or x fixed, respectively, i.e., we specify only the variable which is held fixed. Likewise $\mathbf{z}(t)$ and $\mathbf{z}(x)$ denote respectively the set of nodal values of $z(x, t)$ for t fixed and the time sequence of values for x fixed; $\mathbf{u}(t)$ and $\mathbf{z}(t)$ have dimensions n_0 and n_1 , whereas $\mathbf{u}(x)$ and $\mathbf{z}(x)$ have dimension NT, which is the number of time instants considered in the heart beat. In the following the vectors are taken as column vectors; their transposes, denoted by $\mathbf{z}^*, \mathbf{u}^*, \dots$, are row vectors.

We now examine the structure of the transfer matrix T . Using, as we did, isoparametric elements of order one (2-D on Γ_1 and Γ_0 , 3 D in Ω), the approximation functions are bilinear (trilinear) in the local system of coordinates on each surface (volume) element; the local transformation of a surface (volume) element into a reference square (cube), is of bilinear (trilinear) type (see [8, 22, 32]).

As a basis on Γ_0 we can choose the approximation functions which take the value 1 at one node and 0 at all the others. Denoting by $\phi_j^0(x)$, $j = 1, \dots, n_0$, the basis functions, any element u of the function space on Γ_0 spanned by $\{\phi_j^0, j = 1, \dots, n_0\}$ is defined in terms of its nodal values u_j by the relation

$$u(x, t) = \sum_{j=1}^{n_0} u_j \phi_j^0(x).$$

The time dependence of u is through the nodal components $u_j(t)$ of the vector $\mathbf{u}(t)$. Similar considerations apply to Γ_1 and Ω .

We now solve the problem (1) using the discretized variational formulation [22, 32] with $u = \phi_j^0$, and we denote by $\mathbf{t}_j = (t_{1j}, \dots, t_{n_1 j})^*$ the vector of the nodal values of the approximate solution on Γ_1 . Setting $T = \{\mathbf{t}_1, \dots, \mathbf{t}_{n_0}\}$ and denoting by $\mathbf{u}(t)$ and $\mathbf{z}(t)$ the nodal values of $u(x, t)$ and $z(x, t)$, we have then

$$\mathbf{z}(t) = T\mathbf{u}(t) + \mathbf{e}(t), \quad (2)$$

i.e., the matrix T is an approximation of the transfer operator A , and $\mathbf{e}(t)$ indicates the discretization error.

If we consider a part Σ of the surface Γ_1 , the transfer matrix between Γ_0 and Σ is obtained by keeping only the rows of T related to the nodes of Σ .

We note that the transfer matrix may also be obtained by means of boundary-integral methods [15]. For instance, in [16] a boundary-integral formulation was applied to simulated data; in [2], [20] a finite-element and collocation approximation of the Green formula was used relating to data from in vivo experiments. For a general analysis of integral methods applied to the direct potential problem see [5].

In the present work we computed the transfer matrix by means of the FEM applied to the 3-D variational formulation of the problem (1), since in our experience the FEM is more efficient in terms of CPU time and central storage. Also, in [31] the transfer matrix was computed by a 3-D FEM and was applied to the solution of the inverse problem on simulated data.

We now consider the *inverse problem of electrocardiography* in terms of potential alone. This problem can be formulated as follows:

$$\begin{aligned} \Delta V(x, t) &= 0 && \text{in } \Omega, \\ V(x, t) &= z_e(x, t) && \text{on } \Sigma \subset \Gamma_1, \\ \frac{\partial V(x, t)}{\partial n} &= 0 && \text{on } \Gamma_1. \end{aligned} \quad (3)$$

$z_e(x, t)$ is the potential known on a part Σ of Γ_1 representing the lateral tank surface, and we are particularly interested in determining the trace u of V on Γ_0 , i.e. in estimating the epicardial potential distribution from the knowledge of the thorax potential distribution.

In discrete form and in terms of the transfer matrix T (between Γ_0 and Σ), the above problem can be stated as

$$T\mathbf{u}(t) = \mathbf{z}_e(t), \quad (4)$$

where T has dimension $m \times n_0$, with m the number of nodes on Σ .

Since, as a rule, $m > n_0$, the problem must be solved in the least-squares sense. However, this is not sufficient, since the problem (4) is ill posed, i.e.,

small perturbations present in the measured data $\mathbf{z}_e(t)$ can generate greatly amplified perturbations on $\mathbf{u}(t)$. The ill-posedness of (4) is revealed by the fact that T is an ill-conditioned matrix, i.e., the ratio between the greatest and smallest nonzero singular values of T is quite large, about 10^6 (we recall that the singular values are the square roots of the eigenvalues of T^*T , with T^* the transpose of T).

The problem (4) is solved by means of a regularization technique (see e.g. [27], [30]), previously investigated in [6, 4, 8, 10] and also theoretically treated in [8, 11]. The problem is approximated with the following stable problem dependent on a smoothing or regularization parameter $\epsilon > 0$:

Find $\mathbf{u}_\epsilon(t)$ that minimizes

$$\frac{1}{m} \|T\mathbf{v} - \mathbf{z}_e(t)\|^2 + \epsilon \|R\mathbf{v}\|^2 \quad \text{for all } \mathbf{v} \in \mathbb{R}^{n_0}. \quad (5)$$

The norms $\|\cdot\|$ are the euclidean norms in \mathbb{R}^m and \mathbb{R}^{n_0} respectively, and R is the regularization operator, a matrix which in our case is the FEM approximation of the operator $\text{grad}|_{\Gamma_0}$, the gradient operator on the surface Γ_0 . This choice was based on numerical experiments carried out with this and other regularization operators which indicated a better performance of the gradient operator [8].

In (5), $\mathbf{z}_e(t)$ and $\mathbf{u}_\epsilon(t)$ are considered for a given time instant, and the problem is to be solved for a sequence of time instants during the heart beat. There arises the question of the best choice of the regularization parameter ϵ : if ϵ is too small, the noise on $\mathbf{z}_e(t)$ and the arithmetical noise related to the numerical solution of (5) will cause excessive oscillations in $\mathbf{u}_\epsilon(t)$; on the other hand, if ϵ is too large, $\mathbf{u}_\epsilon(t)$ is excessively smoothed; and in either case no useful information can be obtained from $\mathbf{u}_\epsilon(t)$.

We have considered two cases:

(i) Both the thorax potentials $\mathbf{z}_e(t)$ and the epicardial potentials $\mathbf{u}_e(t)$, known as measurements from the in vitro experiment, are used: ϵ is chosen so as to minimize $\|\mathbf{u}_e(t) - \mathbf{u}_\epsilon(t)\|$. The ϵ so defined is called optimal (OPT), and the corresponding epicardial-potential estimate is denoted by $\mathbf{u}_0(t)$, the optimal estimate (OPTE); $\mathbf{u}_0(t)$ is the best possible reconstruction of $\mathbf{u}_e(t)$ from the actual data $\mathbf{z}_e(t)$.

(ii) Only the measured $\mathbf{z}_e(t)$ is used. In this case the regularization parameter $\epsilon > 0$ is chosen by means of a heuristic criterion, called composite residual and smoothing operator (CRESO). In our experience [9, 10] this criterion has consistently yielded estimates $\mathbf{u}_\epsilon(t)$ in good agreement with the optimal ones; moreover, CRESO does not require *a priori* information about the noise affecting $\mathbf{z}_e(t)$. According to this criterion, ϵ is chosen as the first

point of relative maximum for the function

$$C(\varepsilon) = \|R\mathbf{u}_\varepsilon(t)\|^2 + 2\varepsilon \frac{d}{d\varepsilon} \|R\mathbf{u}_\varepsilon(t)\|^2, \quad (6)$$

and the epicardial estimate so obtained is denoted by $\mathbf{u}_c(t)$.

In both cases (i) and (ii) the choice of the regularization parameter is time dependent.

We remark that the inverse procedure used in [3] on in vivo data and in [16, 31] on simulated data can be obtained from the above-described regularization procedure by choosing the identity matrix as the regularization operator; moreover, in [3] the regularization parameter is kept constant throughout the heart beat.

COMPUTATIONAL METHODS

The discrete surface Γ_1 was defined by the measured coordinates of 400 electrodes distributed on the lateral surface of the thorax-shaped tank plus about 200 nodes distributed on the two flat bases (upper and lower) of the tank. Similarly, the discrete surface Γ_0 was defined by 216 electrode locations plus 7 interpolation points distributed on the upper and lower bases of the epicardial frame. The 3-D mesh connecting the two surface meshes was made up of 1680 hexahedral elements and 2110 nodes.

As previously explained, the computation of the transfer matrix T requires the solution (in discretized form) of the following n_0 direct problems:

$$\Delta V_j = 0 \text{ in } \Omega, \quad V_j = \phi_j^0 \text{ on } \Gamma_0, \quad \frac{\partial V_j}{\partial n} = 0 \text{ on } \Gamma_1, \\ j = 1, \dots, n_0, \quad (7)$$

where ϕ_j^0 are the basis functions on Γ_0 . The columns of the matrix T are the nodal values on Γ_1 of the solution V_j ; if a subset of nodes of Γ_1 is considered, only the nodal values on the subset are retained.

The discrete solution of the n_0 direct problems leads to linear systems characterized by the same symmetric and positive definite matrix. The known vectors of the linear systems coincide successively with the columns of the identity matrix. The n_0 linear systems are solved simultaneously by means of a modified frontal technique (see [14]) which allows one to efficiently solve several systems defined by the same matrix.

The transfer matrix T relating the $n_0 = 230$ epicardial nodes to the $m = 400$ nodes on the thorax-shaped tank was computed by means of a FORTRAN program on a Honeywell DPS8 system requiring a CPU time of about 1 hour and 130 K of core-memory allocation.

Concerning the numerical solution of the regularized least-squares problem (5), we remark that it must be solved for a sequence of time instants, and for each instant some trials are required for choosing the parameter ϵ according to the OPT or CRESO criterion; hence it is important to transform (5) so that it can be solved in a very fast way. This goal can be achieved by means of the generalized singular-value decomposition (GSVD) [28, 29]. Using this decomposition, it is possible to find two orthogonal matrices U, V and an invertible matrix X such that $U^*TX = D_T$, $V^*RX = D_R$, where D_T and D_R are diagonal matrices having the same dimensions of T and R . Taking the properties of the orthogonal matrices into account and setting $\xi = X^{-1}\mathbf{v}$, $\gamma = X^{-1}\mathbf{z}_e$, the problem (5) is transformed into the following problem:

Find $\xi_\epsilon(t)$ that minimizes

$$\frac{1}{m} \|D_T \xi - \gamma\|^2 + \epsilon \|D_R \xi\|^2 \quad \text{for all } \xi \in \mathbb{R}^{n_0}.$$

Then $\mathbf{u}_\epsilon(t) = X\xi_\epsilon(t)$. In this form both the solution of (5) and the choice of ϵ are obtained by a fast and straightforward procedure. The numerical algorithm we used to perform the GSVD requires two Householder triangularizations and one singular-value decomposition. The FORTRAN program implementing this algorithm on the same computer system required 1.8 hours of CPU and 135 K of core-memory allocation for a transfer matrix T with $n_0 = 230$ and $m = 278$ related to a subset of the 400 thorax electrodes.

RESULTS

In this section we denote by t_i , $i = 1, \dots, NT$, the sequence of the time instants of the heart beat, and by x_j , $j = 1, \dots, m$ (or n), the position of the electrodes respectively on the thorax and on the "epicardial" frame at which the potential values are considered.

We recall the notations about the various time-space potential distributions used in the discussion of the results:

$z_e(t_i, x_j)$, $i = 1, \dots, NT$, $j = 1, \dots, m$: the measured thoracic potential distribution;

$z_c(t_i, x_j)$, $i = 1, \dots, NT$, $j = 1, \dots, m$: the simulated thoracic potential distribution;

$u_e(t_i, x_j)$, $i = 1, \dots, NT$, $j = 1, \dots, n$: the measured epicardial potential distribution;

$u_0(t_i, x_j)$, $i = 1, \dots, NT$, $j = 1, \dots, n$: the optimal estimate (OPT-EST) of the epicardial potential distribution;

$u_c(t_i, x_j)$, $i = 1, \dots, NT$, $j = 1, \dots, n$: the CRESO estimate (C-EST) of the epicardial potential distribution.

If $v(t_i, x_j)$, $i = 1, \dots, NT$, $j = 1, \dots, k$, denotes a generic time-space distribution, we consider it, for t fixed, as the spatial vector $\mathbf{v}(t) = (v(t, x_1), \dots, v(t, x_k))^*$, usually referred to as a potential map, or, for x fixed, as the temporal vector $\mathbf{v}(x) = (v(t_1, x), \dots, v(t_{NT}, x))^*$, usually referred to as an ECG. Moreover, for an l -dimensional vector $\mathbf{v} = (v_1, \dots, v_l)^*$ [which may represent either $\mathbf{v}(t)$ or $\mathbf{v}(x)$], we introduce the following notation:

$$\begin{aligned} |\mathbf{v}| &= \left(\frac{1}{l} \sum_{i=1,l} v_i^2 \right)^{1/2}, \\ (\mathbf{v}, \boldsymbol{\omega}) &= \frac{1}{l} \sum_{i=1,l} v_i \omega_i \quad \text{for } \mathbf{v}, \boldsymbol{\omega} \in \mathbb{R}^l, \\ \hat{\mathbf{v}} &= \mathbf{v} - \left(\frac{1}{l} \sum_{i=1,l} v_i \right) \mathbf{e}, \quad \text{where } \mathbf{e} = (1, 1, \dots, 1)^*. \end{aligned}$$

If \mathbf{v}_e and \mathbf{v}_c denote the time-space measured and computed distributions, the comparison between the two will be performed by means of the following accuracy indices:

spatial relative error, at a given time instant t :

$$\text{RE}(t) = \frac{|\mathbf{v}_e(t) - \mathbf{v}_c(t)|}{|\mathbf{v}_e(t)|};$$

temporal relative error, at a fixed location x :

$$\text{RE}(x) = \frac{|\mathbf{v}_e(x) - \mathbf{v}_c(x)|}{|\mathbf{v}_e(x)|};$$

spatial correlation coefficient at fixed t :

$$\text{CC}(t) = \frac{(\hat{\mathbf{v}}_e(t), \hat{\mathbf{v}}_c(t))}{|\hat{\mathbf{v}}_e(t)| \cdot |\hat{\mathbf{v}}_c(t)|};$$

temporal correlation coefficient at fixed x :

$$\text{CC}(x) = \frac{(\hat{\mathbf{v}}_e(x), \hat{\mathbf{v}}_c(x))}{|\hat{\mathbf{v}}_e(x)| \cdot |\hat{\mathbf{v}}_c(x)|};$$

root-mean-square error at fixed t :

$$\text{RMSE}(t) = |\mathbf{v}_e(t) - \mathbf{v}_c(t)|;$$

root-mean-square error at fixed x :

$$\text{RMSE}(x) = |\mathbf{v}_e(x) - \mathbf{v}_c(x)|.$$

In all the tables and in some figures the following notation is used:

$\text{BSM}(t) = |\mathbf{z}_e(t)|$ and $\text{BSM}(x) = |\mathbf{z}_e(x)|$: the magnitude of the measured thoracic potential map (MTPM) and the magnitude of the measured thoracic ECG at location x , respectively;

$\text{SSM}(t) = |\mathbf{z}_c(t)|$ and $\text{SSM}(x) = |\mathbf{z}_c(x)|$: the magnitude of the simulated thoracic potential map (STPM) and the magnitude of the simulated thoracic ECG at location x , respectively;

$\text{EEM}(t) = |\mathbf{u}_e(t)|$ and $\text{EEM}(x) = |\mathbf{u}_e(x)|$: the magnitude of the measured epicardial potential map (MEPM) and the magnitude of the measured epicardial ECG at location x , respectively;

$\text{CEM}(t) = |\mathbf{u}_c(t)|$ and $\text{CEM}(x) = |\mathbf{u}_c(x)|$: the magnitude of the computed epicardial potential map (CEPM) and the magnitude of the computed epicardial ECG at location x , respectively;

$\text{RES}(t) = |T\mathbf{u}_c(t) - \mathbf{z}_e(t)|$: the root-mean-square error between the MTPM and the simulated one from the CEPM;

$\text{MRES}(t) = \min_{v \in \mathbb{R}^I} |T\mathbf{v} - \mathbf{z}_e(t)|$: the residual related to the least-squares solution of $T\mathbf{u} = \mathbf{z}_e(t)$;

$\text{BSRE}(t) = \text{RES}(t)/\text{BSM}(t)$: the relative error of the surface fitting;

$\text{IRE}(t) = \text{RE}_c(t)/\text{RE}_0(t)$: the inefficiency index of the C-EST with respect to the OPT-EST, i.e. the ratio of the RE of each estimate to that of the MEPM;

$\text{ICC}(t) = \text{CC}_0(t)/\text{CC}_c(t)$: the inefficiency index, given by the ratio of the CC of the OPT-EST to that of the C-EST;

$\text{RTE}(t) = \text{EEM}(t)/\text{BSM}(t)$;

$\text{RTC}(t) = \text{CEM}(t)/\text{BSM}(t)$;

$\text{EREG}(t) = \epsilon$: smoothing parameter chosen according to the OPT or CRESO criterion for each instant.

For each of the symbols listed above, the space or time variable is omitted whenever it can be clearly inferred from the context. Moreover, a bar over the symbol [e.g. $\overline{\text{RE}}(t)$ or $\overline{\text{RE}}(x)$] means that the related quantity has been averaged over the corresponding variable range.

TESTS OF THE NUMERICAL PROCEDURES

To check the correctness of the implemented procedures and to investigate the influence of the discretization error, due to the FEM approximation, on the accuracy of the inverse solution, we performed some numerical experi-

ments with the following test functions:

$$\phi(x, y, z) = \begin{cases} F1 = a_1 \tilde{y} \tilde{z} + b_1 \tilde{x} \tilde{y} / r^5, \\ F2 = \tilde{x} \tilde{z} + b_2 \tilde{y} / r^3, \end{cases}$$

with $r^2 = \tilde{x}^2 + \tilde{y}^2 + \tilde{z}^2$, $\tilde{x} = x - x_0$, $\tilde{y} = y - y_0$, $\tilde{z} = z - z_0$.

The location of (x_0, y_0, z_0) was the center of the fourth circumference from the bottom of the “epicardial” cage; moreover we chose $a_1 = 0.25$, $b_1 = 10^5$, and $b_2 = 5 \times 10^3$. The functions F1 and F2 behave respectively like a quadrupolar and a dipolar source, and since the singularity (x_0, y_0, z_0) was inside the domain bounded by Γ_0 , ϕ was harmonic in Ω .

Setting

$$u_e = \phi|_{\Gamma_0}, \quad g = \frac{\partial \phi}{\partial n} \Big|_{\Gamma_1} \neq 0, \quad z_e = \phi|_{\Sigma},$$

where Σ denotes the lateral surface of the tank, and considering the solutions \mathbf{u}, W of

$$\begin{aligned} \Delta U = 0 \text{ in } \Omega, \quad U|_{\Gamma_0} = u_e, \quad \frac{\partial U}{\partial n} \Big|_{\Gamma_1} = 0, \\ \Delta W = 0 \text{ in } \Omega, \quad W|_{\Gamma_0} = 0, \quad \frac{\partial W}{\partial n} \Big|_{\Gamma_1} = g, \end{aligned} \tag{9}$$

we have $\phi = U + W$. Hence it follows that $z_e = Au_e + W|_{\Sigma}$, where A is the transfer operator between Γ_0 and Σ related to the problem (1). Denoting by \mathbf{z}_e the vector of the nodal values of ϕ on the thorax nodes of Σ and by \mathbf{u}_e the vector of the nodal values of u_e on the 230 epicardial nodes, we set $\mathbf{z} = \mathbf{z}_e + \boldsymbol{\eta}$, where $\boldsymbol{\eta}$ is a noise vector of pseudorandom variables normally distributed with zero mean and common variance σ^2 .

We consider the inverse problem of recovering \mathbf{u}_e given \mathbf{z} , for different values of the signal-to-noise ratio $S/N = \|\mathbf{z}_e\|/\|\boldsymbol{\eta}\|$. Then the corresponding regularized estimate \mathbf{u}_e is the solution of

$$\frac{1}{m} \|T_0 \mathbf{u}_e - \mathbf{z}\|^2 + \varepsilon \|R \mathbf{u}_e\|^2 = \min_{v \in \mathbb{R}^n} \left[\frac{1}{m} \|T_0 v - \mathbf{z}\|^2 + \varepsilon \|R v\|^2 \right],$$

where $T_0 v = T v + \mathbf{w}$ and \mathbf{w} is the vector of the nodal values on Σ of the FEM approximation of W , the solution of Equation (9). The regularization parameter ε was chosen according to the OPT or CRESO criterion.

In Table 1 we report the accuracy indices related to the comparison of \mathbf{z}_e with the simulated data $\mathbf{z}_e = T \mathbf{u}_e + \mathbf{w}$.

TABLE 1

Direct Problem on Test Functions

ϕ	RE	CC	RMSE	BSM	SSM	EEM	TRE
F1	7.11E-2	0.998	2.92	41.06	39.80	375	7.6E-2
F2	2.35E-2	0.99990	1.72	72.87	73.16	163	3.3E-2

From Table 1 we deduce an estimate of the error related to the discretization process, which in terms of the relative error RE is 2.4 and 7 percent, and in terms of RMSE is at most 3. The total relative error (TRE) computed on all the nodes of the 3-D mesh is also reported.

The inverse results reported in Table 2 imply that in the presence of the discretization error only ($\sigma = 0$), the RE of the information recovered by means of the CRESO criterion ranges from 0.14 to 0.24. In Table 2, the numbers with an asterisk in the column headed S/N are the root-mean-square errors between the \mathbf{z}_e data and the values predicted on the surface from the data recovered on the "epicardial" frame. Increasing the S.D. σ of the noise affecting the thorax data \mathbf{z} , we see that the correlation coefficient (CC) does not decrease as rapidly as RE increases; moreover, we find that with S/N ranging between 2 and 12 the information on the epicardial frame is recovered with an RE and a CC ranging over 0.15–0.36 and 0.93–0.99 respectively.

TABLE 2

Inverse Problem on Test Functions

σ		$\phi = F1$			$\phi = F2$		
		RE	CC	S/N	RE	CC	S/N
0	OPT-EST	0.223	0.975	0.81*	0.133	0.992	0.44*
	C-EST	0.241	0.970	0.69*	0.141	0.990	0.42*
0.25	OPT-EST	0.224	0.974	170	0.132	0.992	218
	C-EST	0.242	0.970		0.139	0.991	
5	OPT-EST	0.253	0.968	8.9	0.154	0.989	12
	C-EST	0.259	0.966		0.154	0.989	
7	OPT-EST	0.261	0.966	6.0	0.181	0.985	7.8
	C-EST	0.262	0.965		0.182	0.985	
10	OPT-EST	0.298	0.956	4.1	0.218	0.979	5.9
	C-EST	0.304	0.953		0.219	0.978	
20	OPT-EST	0.358	0.934	2.1	0.233	0.973	2.9
	C-EST	0.364	0.932		0.255	0.967	

These results show that in presence of realistic S/N ratios, the recovered information is of high quality with a rather satisfactory accuracy in terms of RE. As previously stated, the inverse problem is strongly ill posed. The numerical findings suggest that, in the presence of the discretization errors and a realistic noise level on the data, what can be pursued in these inverse calculations is a good recovery of the epicardial patterns, but not an equally satisfactory numerical accuracy.

Finally, the results reported in Table 2 show that the regularization algorithm, with the CRESO choice of ϵ , performed very well, yielding estimates comparable with the best recoverable epicardial information (OPT-EST).

DIRECT PROBLEM: ANALYSIS OF A NORMAL HEART BEAT

The numerical solution of the direct problem was calculated by using the potential values measured at $n = 216$ points located on the lateral surface of the epicardial frame and by attributing interpolated values at seven interior nodes on the lower and upper circular basis of the frame. Hence the experimental epicardial maps $\mathbf{u}_e(t)$ were defined by 230 potential values distributed on the epicardial frame.

We then computed the simulated thoracic maps $\mathbf{z}_c(t) = T\mathbf{u}_e(t)$ and compared $\mathbf{z}_c(t)$ with $\mathbf{z}_e(t)$ at the $m = 278$ thorax nodes chosen among the 400 locations of the thorax electrodes. Some locations on the lower part of the thorax, and some others where the lead contact was poor, were excluded.

The direct problem was solved for about $NT = 170$ time instants 2 msec apart, relating to a normal heart beat.

In Figure 4 we report the time behavior of the magnitude of the MEPM and of the MTPM respectively, which shows three peaks corresponding to the P , QRS , and T waves. The onset and durations of the waves were approximately determined from a reference ECG. We remark that the average ratio between these two magnitudes over the heart beat is 2.5, and this ratio is sometimes higher than 3, especially in the QRS interval.

From Figure 5(a) we see that the magnitude of the simulated and measured thorax maps exhibits a very similar time course, with an overestimate of the simulated maps at the peaks of the P , QRS , and T waves. Figure 5(b) shows the $RMSE(t)$ between the experimental and simulated thorax maps. Setting $\mathbf{z}_e(t) = \tilde{\mathbf{z}}_e(t) + \mathbf{e}_T(t)$, $\mathbf{u}_e(t) = \tilde{\mathbf{u}}_e(t) + \mathbf{e}_H(t)$, where $\mathbf{e}_T(t), \mathbf{e}_H(t)$ denote the errors affecting the thorax and the epicardial measured data respectively, and $\tilde{\mathbf{z}}_e(t), \tilde{\mathbf{u}}_e(t)$ denote the exact data, then the error between the measured and computed thorax maps can be split into the following three components:

$$\begin{aligned}\delta(t) &= \mathbf{z}_e(t) - T\mathbf{u}_e(t) = \tilde{\mathbf{z}}_e(t) - T\tilde{\mathbf{u}}_e(t) + \mathbf{e}_T(t) - T\mathbf{e}_H(t) \\ &= \mathbf{e}_D(t) + \mathbf{e}_T(t) - T\mathbf{e}_H(t),\end{aligned}$$

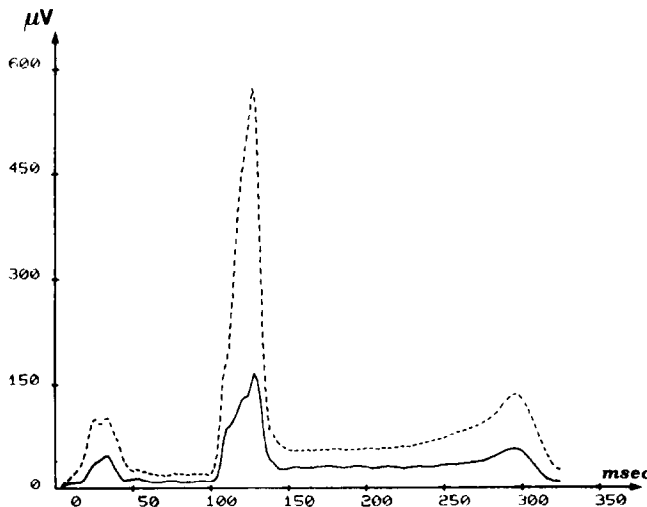


FIG. 4. Time course of $BSM(t)$ (solid line) and $EEM(t)$ (dashed line).

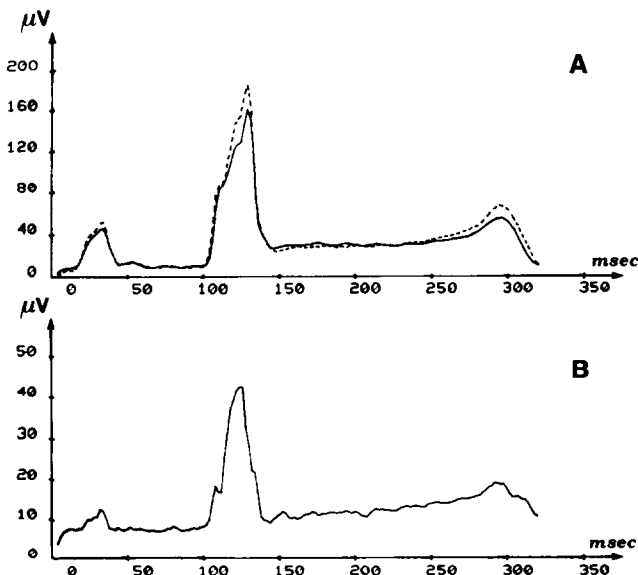


FIG. 5. Time course of: (a) $BSM(t)$ (solid line) and $ssm(t)$ (dashed line); (b) $RMSE(t)$.

where \mathbf{e}_D indicates the part of the error due to the discretization procedure of the Laplace equation used for building up the transfer matrix.

The results in Table 1 suggest that, due to the discretization error, the simulated surface potential distribution is expected to have at most a RE of 0.1. Considering an average magnitude of measured thorax maps of 30 μV (as in the P and ST intervals), a rough estimate of 3 μV is obtained for the magnitude of the component \mathbf{e}_D in the RMSE error due to the discretization error source. The data $\mathbf{z}_e(t)$ and $\mathbf{u}_e(t)$ are both affected by an electronic and quantization noise level whose S.D. is about 5–6 μV ; moreover, an epicardial white-noise map \mathbf{e}_H of S.D. 5–6 μV produces a computed surface map $T\mathbf{e}_H$ having a magnitude less than 1 μV . Hence, considering the previous components of the RMSE error as independent sources of noise, we obtain that these three sources of error yield an estimate for the RMSE error of 6–7 μV . This estimate covers a large part of the RMSE error obtained in the P , PQ , and ST intervals, which amounts to 7–12 μV , as shown in Table 3.

In fact, in these time intervals the source of noise related to the time alignment and A.D. conversion of the measured data is small, due to the low values and weak temporal variation of the potential. On the other hand, in the QRS and T waves we obtain an average RMSE of 22 and 16 μV respectively (Table 3), which reveals that errors caused by time alignment and A.D. conversion are larger, due to the steepness of the signals in these waves, as shown in Figure 4.

Figure 6(a) and (b) display the time behavior of $\text{CC}(t)$ and $\text{RE}(t)$, showing that good accuracy and the best pattern match are obtained in the P , QRS , ST , and T intervals, as the average values in Table 3 also indicate, whereas in the PQ interval we have a loss of accuracy and pattern match. This could be expected because of the small magnitude of the signal, which has an average value of 10 μV , comparable with the *a priori* estimate of the RMSE error due to the electronic noise and to the discretization error.

TABLE 3
Direct Problem: Average Values of Magnitudes and
Accuracy Indices of Simulated Thorax Maps

Interval			$\overline{\text{RE}}(t)$	$\overline{\text{RMSE}}(t)$	$\overline{\text{CC}}(t)$	$\overline{\text{BSM}}(t)$	$\overline{\text{SSM}}(t)$
(msec)	Complex						
20–44	P		0.341	9.521	0.935	31.327	34.462
46–102	PQ		0.708	7.584	0.678	10.886	11.026
104–150	QRS		0.307	22.181	0.957	79.189	88.441
152–248	ST		0.391	11.912	0.915	30.465	29.348
250–308	T		0.387	16.012	0.943	42.019	48.880
104–308	$QRST$		0.370	15.499	0.933	45.183	48.807
20–308	$PQRST$		0.435	13.380	0.882	37.082	39.964

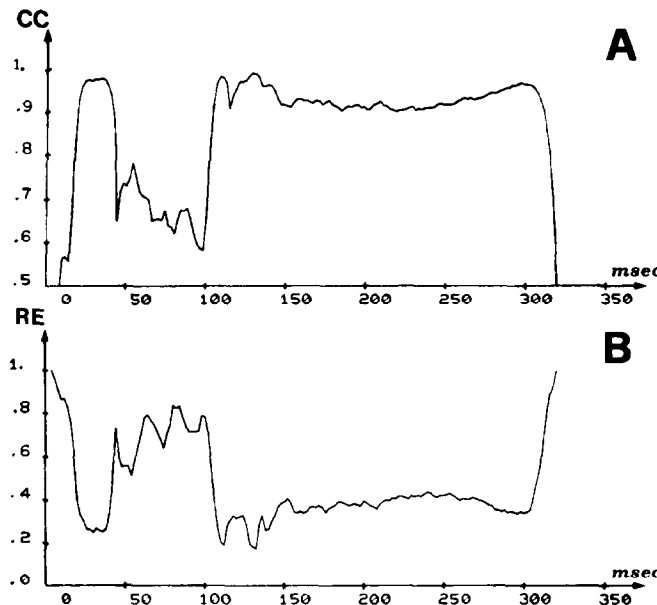


FIG. 6. Time behavior of (a) $CC(t)$ and (b) $RE(t)$.

We present here a few examples of the results of the direct procedure. Measured and simulated potential maps were automatically drawn as a set of equipotential lines on a Tektronix 4012 graphic display.

Figure 7 (top) shows the instantaneous distribution of equipotential lines on the surface of the torso-shaped tank during atrial excitation (P wave). Due to the considerable attenuation of the signal in the highly conductive medium, the S/N ratio is rather low, particularly in some areas.

Figure 7 (bottom) displays the surface distribution simulated from the epicardial measurements. The correlation between the two images is excellent ($CC = 0.98$). Since the simulated map is not affected by thoracic-measurement noise, it displays a greater regularity than the measured one. Moreover, since the RMSE between the two maps is about $1 \mu\text{V}$, close to its *a priori* estimate, the simulated data can be considered as the result of a filtering procedure.

Similar considerations apply to the subsequent images (Figures 8 and 9) relating to ventricular excitation. Both the simulated and measured maps display features which can be correlated with intraventricular events, namely right ventricular breakthrough and separate excitation waves traveling through the right and left ventricular myocardium (Figure 9). A fairly simple repolarization pattern is illustrated in Figure 10.

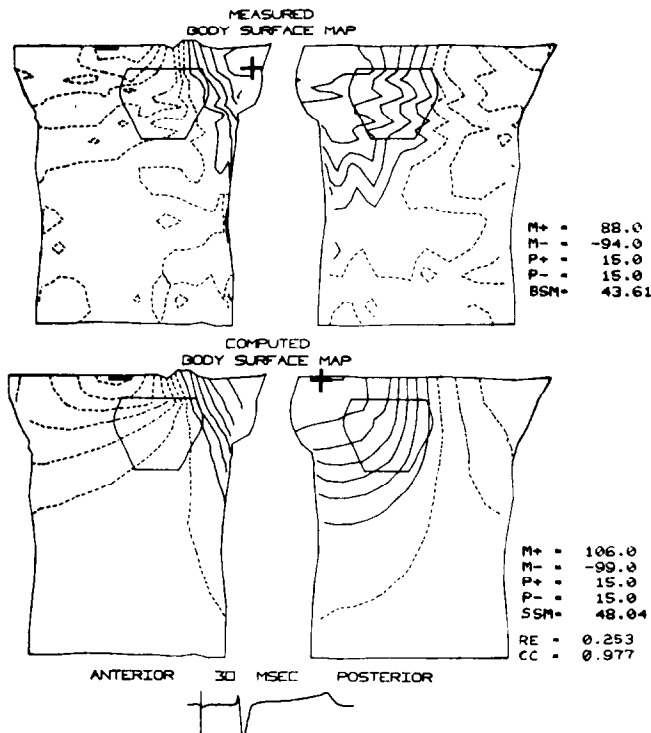


FIG. 7. Measured thorax maps (top panel) and those simulated by solving the direct problem (bottom panel) displayed by means of equipotential lines. Solid (dashed) lines indicate positive (zero or negative) equipotential lines; the sign + (-) the absolute maximum (minimum), whose numerical value in μV is given on the side by $M+$ ($M-$) together with the voltage step $P+$ ($P-$). A vertical line on the electrocardiogram indicates the time instant considered. The following Figures 8, 9, 10 show measured and simulated thorax potentials at three successive time instants.

The simulated data, related to 170 successive instantaneous body surface maps, were used to obtain a simulated ECG for each electrode location.

In Table 4 we report the average of the accuracy indices $RE(x)$ and $CC(x)$ between the simulated and measured ECG related to 278 chest points. These indices were computed for different time intervals during the heart beat. Over the entire heart beat a good accuracy and pattern match for the simulated ECGs was obtained; from Table 4 we deduce that the accuracy is quite good in the *QRS* interval and the patterns match reasonably well in the *P* and *T* waves.

Unsatisfactory results are obtained in the *PQ* and *ST* intervals. In these intervals the magnitude of the epicardial and thorax maps is almost constant,

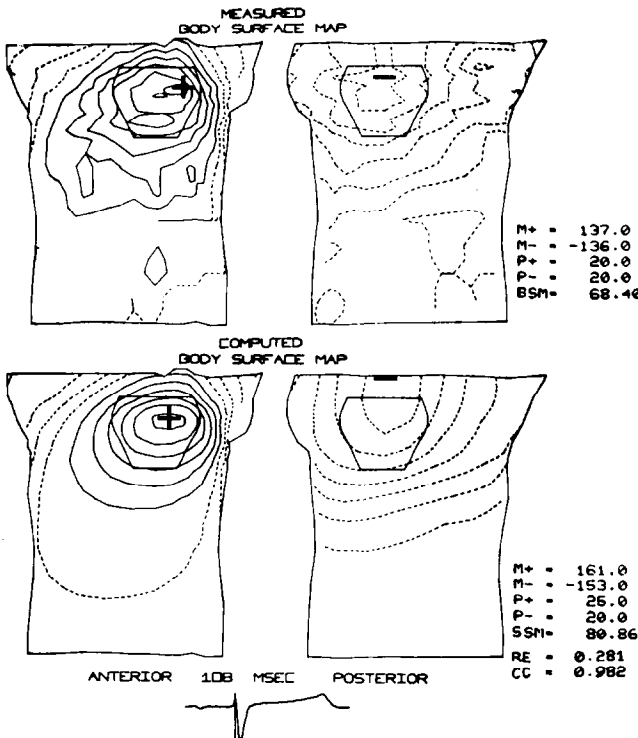


FIG. 8. See Figure 7.

as shown in Figure 4, and also the ECGs are fairly constant in time; in both cases the measured potential values at the thorax nodes are constant within the noise level, with a S.D. of 5–6 μ V. Since in the *PQ* interval the average magnitude of the measured thorax ECGs is 9 μ V (see Table 4), which is comparable to the *a priori* estimate of the RMSE error due to the electronic and discretization errors (6–7 μ V), poor accuracy was to be expected. Also, in the *ST* interval the ECGs are almost constant, although changing with the location on the thorax and epicardial surface. This indicates quasistationary potential distributions which were simulated very well, as shown in Table 3. However, the time analysis yields poor results, especially with regard to the pattern match as measured by the CC. Actually the CC is practically meaningless when comparing constant values affected by a random noise. These considerations may explain the loss of accuracy of the pattern match index for the *PQ* and *ST* intervals.

The spatial distribution on the thorax of $CC(x)$ and $RE(x)$, related to the comparison of ECG waveforms over the entire heart beat (Table 5), shows

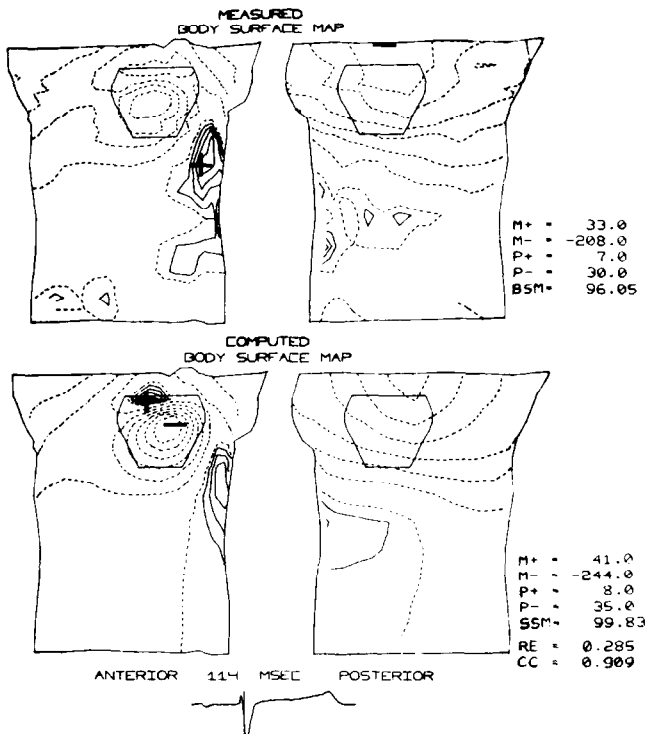


FIG. 9. See Figure 7.

that measured and computed ECGs on the thorax are in good agreement, especially in terms of pattern match. The CC is greater than 0.98 and RE is less than 0.30 in a large anterior and posterior region where the results are better than average. This also holds true for the P, QRS, and T intervals.

The excellent agreement between measured and computed chest ECGs is illustrated by a few representative examples reported in Figure 11. The computed ECGs tend to present higher peaks and to be smoother than the measured ones.

In summary, we have two measures of accuracy: one in time when we compare the ECGs, and one in space when we compare surface maps at a given time instant. The accuracy analysis of the first kind yields slightly better results than the second.

The good agreement between simulated and measured ECGs also constitutes an *a posteriori* validation of the assumption of a quasistatic electric field which has been used for solving the direct problem. As a consequence of the quasistatic assumption the transfer matrix is time independent and is

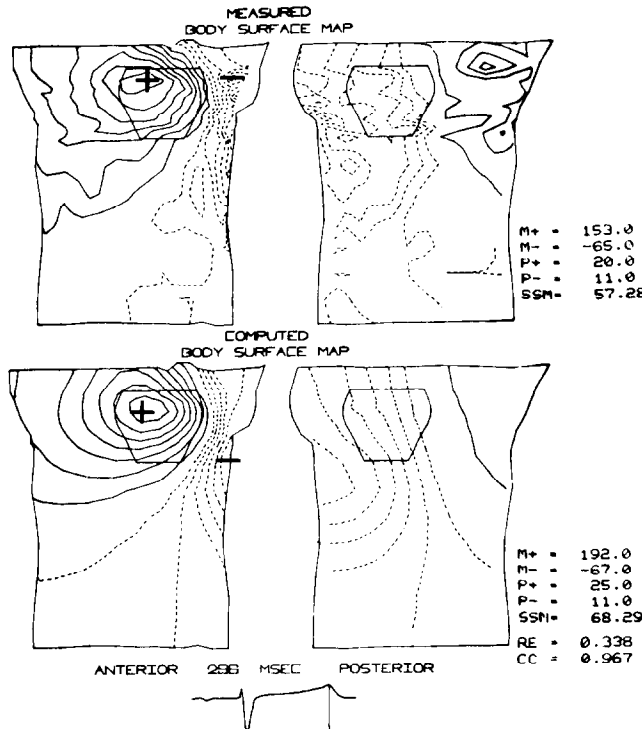


FIG. 10. See Figure 7.

TABLE 4

Direct Problem: Average Values of Magnitudes and Accuracy Indices of Simulated Thorax Maps

Interval (msec)	Complex	$\overline{BSM(x)}$	$\overline{SSM(x)}$	$\overline{RMSE(x)}$	$\overline{RE(x)}$	$\overline{CC(x)}$
20-44	P	29.13	31.29	8.70	0.431	0.834
46-102	PQ	9.52	9.27	6.93	0.957	0.381
104-150	QRS	84.44	93.97	21.99	0.276	0.975
152-248	ST	25.39	24.39	10.13	0.612	0.524
248-308	T	35.58	39.92	12.79	0.538	0.839
104-308	QRST	50.26	55.04	15.11	0.339	0.961
20-308	PQRST	43.74	47.90	13.53	0.349	0.958

TABLE 5

Accuracy Indices between Measured and Simulated Thorax ECGs^a

CC(x)															
A	0.97	0.96	0.97	0.99	0.98	0.95	0.94	0.94	0.92	0.96	0.95	0.95	0.95	0.95	0.95
	0.97	0.96	0.98	0.99	0.99	0.97	0.95	0.95	0.95	0.93	0.98	0.	0.97		
	0.98	0.97	0.97	0.98	0.99	0.98	0.98	0.97	0.97	0.97	0.91	0.91	0.92		
	0.97	0.97	0.97	0.98	0.99	0.99	0.99	0.99	0.99	0.97	0.94	0.93	0.92		
	0.98	0.97	0.97	0.98	0.99	1.00	1.00	0.99	0.99	0.97	0.97	0.93	0.95		
	0.97	0.98	0.97	0.98	0.99	0.99	1.00	0.99	0.99	0.98	0.97	0.96	0.94		
	0.97	0.97	0.96	0.97	0.99	1.00	1.00	0.99	0.99	0.98	0.98	0.97	0.97		
	0.97	0.97	0.95	0.97	0.99	0.99	1.00	0.99	0.98	0.97	0.	0.97	0.96		
	0.95	0.96	0.96	0.	0.99	0.99	0.99	0.99	0.98	0.	0.98	0.99	0.98		
	0.96	0.97	0.96	0.98	0.99	0.99	0.99	0.99	0.98	0.98	0.96	0.97	0.98		
	0.92	0.94	0.95	0.94	0.97	0.99	0.98	0.98	0.98	0.97	0.95	0.95	0.97	0.97	
	0.90	0.92	0.91	0.94	0.91	0.	0.93	0.	0.88	0.90	0.88	0.88	0.93		
	0.84	0.81	0.83	0.86	0.82	0.84	0.86	0.82	0.71	0.66	0.60	0.66	0.81		
P	0.95	0.95	0.97	0.97	0.97	0.98	0.	0.98	0.99	0.98	0.98	0.97	0.97	0.97	
	0.97	0.98	0.98	0.97	0.98	0.98	0.98	0.99	0.99	0.98	0.94	0.98	0.97		
	0.92	0.97	0.96	0.98	0.98	0.98	0.98	0.99	0.99	0.99	0.98	0.98	0.98		
	0.92	0.96	0.97	0.98	0.97	0.98	0.	0.99	0.99	0.99	0.98	0.98	0.97		
	0.95	0.90	0.	0.97	0.98	0.98	0.99	0.99	0.99	0.99	0.99	0.99	0.99	0.98	
	0.94	0.97	0.97	0.98	0.97	0.99	0.99	0.99	0.99	0.99	0.98	0.98	0.98	0.97	
	0.97	0.97	0.97	0.98	0.98	0.98	0.98	0.98	0.98	0.98	0.98	0.98	0.98	0.97	
	0.96	0.97	0.97	0.98	0.98	0.98	0.99	0.98	0.98	0.98	0.98	0.98	0.98	0.97	
	0.98	0.94	0.98	0.98	0.98	0.98	0.98	0.99	0.99	0.99	0.98	0.98	0.97	0.95	
	0.98	0.97	0.98	0.98	0.	0.98	0.99	0.99	0.98	0.98	0.97	0.97	0.95	0.96	
	0.97	0.96	0.97	0.98	0.97	0.97	0.98	0.98	0.98	0.98	0.97	0.96	0.95	0.92	
	0.93	0.92	0.94	0.95	0.96	0.95	0.96	0.96	0.96	0.95	0.88	0.91	0.90	0.90	
	0.81	0.81	0.83	0.	0.89	0.89	0.92	0.90	0.90	0.90	0.	0.83	0.85	0.84	
RE(x)															
A	0.35	0.31	0.29	0.29	0.25	0.56	0.50	0.41	0.59	0.35	0.35	0.42	0.28		
	0.26	0.28	0.31	0.17	0.16	0.26	0.31	0.48	0.68	0.62	0.70	0.	0.21		
	0.32	0.31	0.30	0.22	0.14	0.23	0.28	0.45	0.46	0.86	0.99	0.56	0.39		
	0.32	0.38	0.32	0.19	0.16	0.18	0.35	0.47	0.57	0.56	0.90	0.60	0.38		
	0.24	0.26	0.23	0.19	0.16	0.18	0.26	0.39	0.52	0.56	0.54	0.62	0.38		
	0.25	0.25	0.27	0.19	0.14	0.19	0.24	0.38	0.44	0.45	0.39	0.42	0.38		
	0.31	0.29	0.31	0.24	0.15	0.10	0.25	0.33	0.38	0.31	0.37	0.38	0.32		
	0.27	0.35	0.31	0.27	0.20	0.12	0.18	0.29	0.33	0.37	0.	0.27	0.32		
	0.40	0.27	0.29	0.	0.15	0.12	0.26	0.33	0.35	0.	0.29	0.26	0.30		
	0.35	0.30	0.34	0.27	0.19	0.15	0.17	0.26	0.32	0.25	0.28	0.32	0.29		
	0.43	0.35	0.42	0.37	0.47	0.17	0.32	0.33	0.41	0.30	0.75	0.52	0.31		
	0.55	0.45	0.44	0.52	0.80	0.	0.72	0.	0.92	0.69	0.97	0.59	0.32		
	0.54	0.77	0.95	0.65	0.88	0.74	0.74	0.56	0.54	0.54	0.96	0.68	1.26		
P	0.28	0.27	0.24	0.26	0.24	0.21	0.	0.22	0.32	0.24	0.24	0.43	0.35		
	0.21	0.25	0.23	0.28	0.20	0.23	0.19	0.19	0.19	0.22	0.70	0.20	0.26		

0.39	0.25	0.30	0.24	0.21	0.24	0.20	0.21	0.24	0.18	0.29	0.23	0.32
0.38	0.26	0.24	0.19	0.23	0.20	0.	0.22	0.20	0.21	0.24	0.22	0.32
0.38	0.61	0.	0.21	0.19	0.18	0.18	0.20	0.20	0.21	0.20	0.26	0.24
0.38	0.26	0.23	0.22	0.24	0.19	0.19	0.21	0.19	0.23	0.23	0.23	0.25
0.32	0.27	0.22	0.42	0.20	0.20	0.21	0.24	0.20	0.24	0.21	0.25	0.31
0.32	0.28	0.25	0.18	0.20	0.19	0.18	0.19	0.22	0.23	0.23	0.27	0.27
0.30	0.43	0.26	0.26	0.37	0.19	0.21	0.21	0.25	0.22	0.27	0.24	0.40
0.29	0.25	0.33	0.27	0.	0.40	0.20	0.29	0.25	0.31	0.32	0.53	0.35
0.31	0.56	0.55	0.25	0.55	0.28	0.35	0.29	0.25	0.30	0.32	0.35	0.43
0.32	0.47	0.37	0.57	0.29	0.49	0.31	0.27	0.32	0.55	0.43	0.46	0.55
1.26	0.69	0.60	0.	0.39	0.39	0.53	0.63	0.97	0.	0.96	0.87	0.54

^aOn the anterior (A) and posterior (P) thorax. The values are ordered as the first (from top) 13 rows of 24 electrodes on the thorax-shaped tank. The first column in A (right side of the chest) is repeated as last column in P and vice versa. The 12 zero values indicate leads with poor electric contact. The figures are rounded off to two decimals.

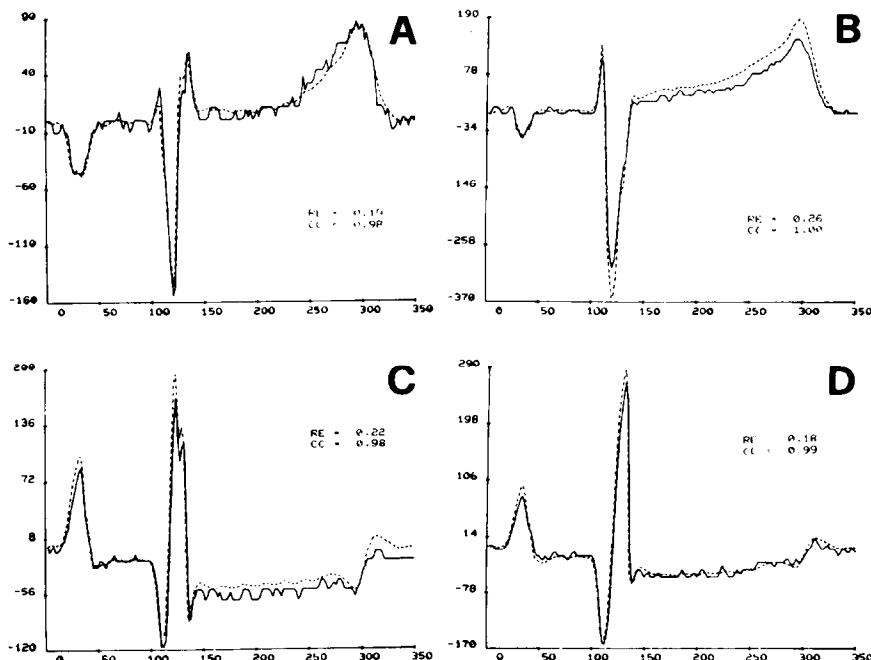


FIG. 11. Comparison between measured (solid lines) and simulated (dashed lines) ECGs at four different lead locations on the thorax; namely, right (a) and middle (b) anterior sites; left (c) and middle (d) posterior sites.

related only to the discretization of the thorax, the epicardial surfaces, and the 3-D medium.

INVERSE PROBLEM: ANALYSIS OF A NORMAL HEART BEAT

We have applied the numerical inverse procedure to the experimental thorax maps $\mathbf{z}_e(t)$, each constituted by $m = 278$ potential values; we computed the epicardial maps using the optimal (OPT) and the CRESO estimate of the regularization parameter ϵ . The accuracy indices between estimated and measured epicardial maps were compared at $n = 212$ points of the epicardial frame, after excluding the nodes on the two bases of the frame and four leads with bad electrical contacts.

In Table 6 we report the average values of various indices over some intervals of the heart beat related to the OPT estimate of ϵ . From the table we deduce that a good pattern match between computed and measured epicardial maps is obtained in the *P*, *QRS*, *ST*, and *T* intervals even if the average RE is about 0.5. These results show that in the presence of the actual noise level on the data it is possible to recover, with a good level of fidelity, the patterns of the potential maps, i.e. features like the locations of maxima or minima and the contours of equipotential lines (see Figures 18–21 below). We remark that the comparison is also affected by the error in the measured epicardial maps, chiefly during the *QRS* and *T* waves, where the time-alignment errors may overcome the instrumentation noise.

Table 7 reports the average of the accuracy indices related to the comparison between the measured maps and the CRESO estimate of the epicardial maps. These results show a very good performance of the CRESO estimates compared to the OPT estimates. The efficiency of CRESO is brought out by the ratio ICC between the CCS related to the optimal and CRESO estimates, which is 1.004 on average over the entire beat.

TABLE 6

Inverse Problem: Average Values of Magnitudes and Accuracy Indices
of the Optimal Estimates of the Epicardial Maps

Interval (msec)	Complex	RE(t)	RES(t)	CC(t)	EEM(t)	CEM(t)	BSRE(t)	EREG(t)
20–44	<i>P</i>	0.498	6.441	0.859	81.419	64.559	0.232	0.201E-04
46–102	<i>PQ</i>	0.691	6.413	0.708	23.065	13.790	0.585	0.356E-03
104–150	<i>QRS</i>	0.487	7.571	0.873	245.357	201.279	0.134	0.182E-04
152–248	<i>ST</i>	0.564	8.135	0.834	59.088	47.256	0.258	0.804E-04
250–308	<i>T</i>	0.446	8.434	0.901	101.338	79.035	0.200	0.287E-04
104–308	<i>QRST</i>	0.511	8.091	0.862	114.796	92.401	0.212	0.509E-04
20–308	<i>PQRST</i>	0.546	7.607	0.831	93.457	74.182	0.289	0.109E-03

TABLE 7
Inverse Problem: Average Values of Magnitudes and Accuracy Indices
of the CRESO Estimates of the Epicardial Maps

Interval (msec)	Complex	$\overline{RE(t)}$	$\overline{RES(t)}$	$\overline{CC(t)}$	$\overline{EEM(t)}$	$\overline{CEM(t)}$	$\overline{BSRE(t)}$	$\overline{EREG(t)}$	$\overline{IRE(t)}$	$\overline{ICC(t)}$
20-44	P	0.502	6.450	0.858	81.419	64.116	0.232	0.206E-04	1.009	1.002
46-102	PQ	0.700	6.486	0.710	23.065	12.903	0.592	0.857E-03	1.012	0.998
104-150	QRS	0.496	7.600	0.869	245.357	202.016	0.136	0.358E-04	1.019	1.005
152-248	ST	0.581	8.377	0.825	59.088	45.344	0.266	0.281E-04	1.031	1.011
250-308	T	0.448	8.437	0.899	101.338	78.965	0.200	0.317E-04	1.006	1.001
104-308	QRST	0.522	8.214	0.857	114.796	91.643	0.216	0.151E-04	1.021	1.007
20-308	PQRST	0.556	7.710	0.828	93.457	73.427	0.293	0.281E-03	1.018	1.004

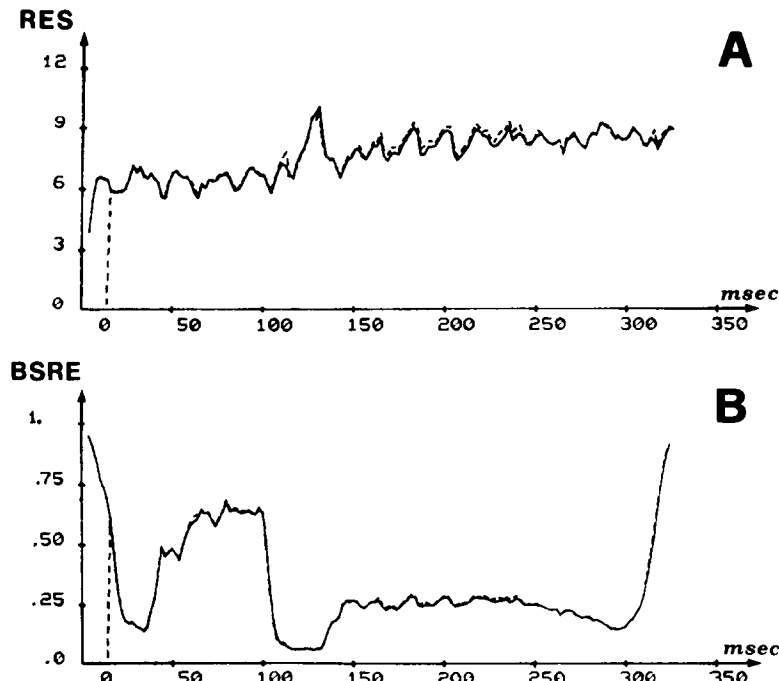


FIG. 12. Time behavior of (a) $\text{RES}(t)$ and (b) $\text{BSRE}(t)$ related to optimal (solid lines) and CRESO (dashed lines) estimates of epicardial potentials.

We now discuss the time course of the accuracy indices throughout the heart beat.

Figure 12(a) shows the time behavior of $\text{RES}(t)$ (the root-mean-square error between the measured body surface maps and those predicted by the optimal or CRESO epicardial estimates). This error amounts to about $8 \mu\text{V}$ on average and presents a peak of about $10 \mu\text{V}$ in the *QRS* complex.

Figure 12(b) displays $\text{BSRE}(t) = \text{RES}(t)/\text{BSM}(t)$, which shows three minima related to the *P*, *QRS*, and *T* waves. The average values related to the same intervals are 0.23, 0.14, and 0.20. We remark that the $\text{RES}(t)$ of CRESO has a time behavior very similar to that related to the OPT estimate.

Setting the regularization parameter $\epsilon = 10^{-6}$, Figure 13(a) and (b) show the variation of α in comparison with the OPT and CRESO estimates; these plots indicate that the values of ϵ range between 10^{-6} and 10^{-3} during the heart cycle with comparatively small variations over the *P* and *T* intervals.

Figures 14 and 15 display the time behavior of CC and RE in comparison with the OPT and CRESO estimates with respect to the measured epicardial

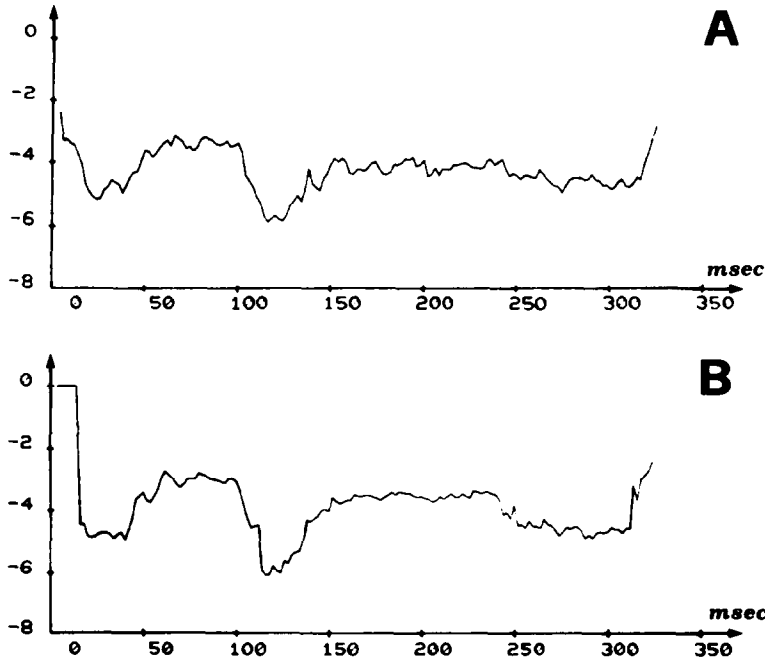


FIG. 13. Time course of $\log_{10} \text{EREG}(t)$ as chosen by the optimal (a) and the CRESO (b) criterion.

maps, showing good qualitative performance of the CRESO estimates. We recall that the CRESO criterion uses only the information contained in MTPM, but does not require a knowledge either of MEPM or of the statistical features of the noise affecting MTPM.

A quantitative comparison of the CRESO and OPT performance in terms of RE is given in Figure 16(a): the CRESO criterion fails only at a few instants at the beginning of the heart beat, and CRESO epicardial estimates yield almost everywhere an RE which is less than 1.1 times the RE of the OPT estimate. Figure 16(b) shows that CRESO performance is better in terms of CC, which is almost everywhere greater than 0.98 times the CC of the OPT estimates. The formulation of the new criterion CRESO was motivated by the fact that other well-known criteria, such as the empirical quotient and sensitivity criteria (see [27, pp. 87–94]), did not perform satisfactorily when applied to our data.

From Figure 17 we deduce that the magnitudes of the OPT and CRESO epicardial estimates have a time behavior very similar to that of the magnitude of the measured epicardial maps; however, the computed magnitude is always somewhat smaller than the measured magnitude.

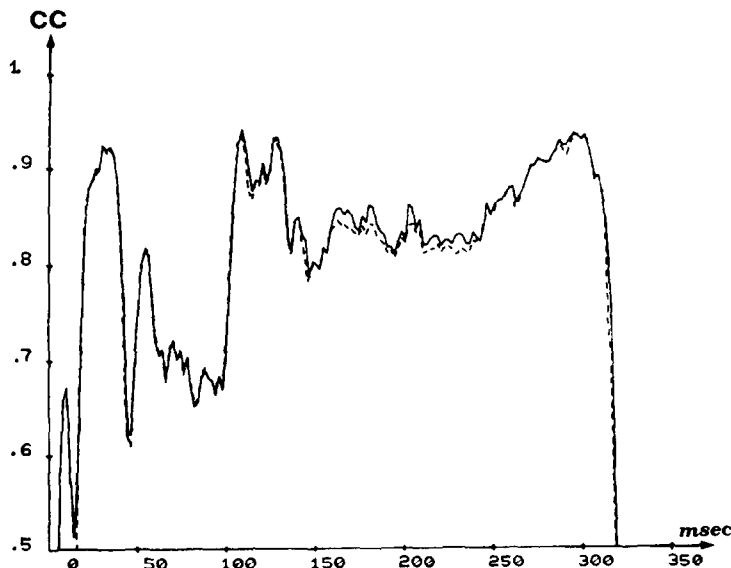


FIG. 14. Time course of $CC(t)$ of epicardial maps estimated by the optimal (solid line) and the CRESO (dashed line) criterion.

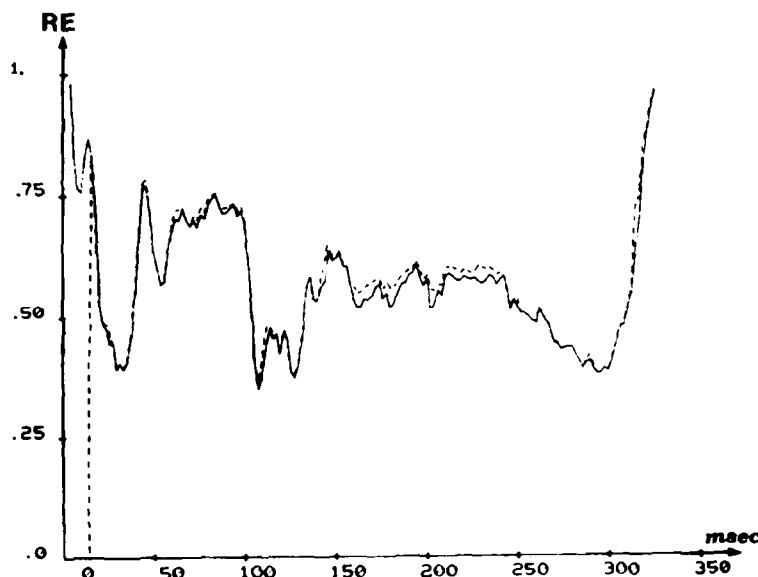


FIG. 15. Time course of $RE(t)$ of epicardial maps estimated by the optimal (solid line) and the CRESO (dashed line) criterion.

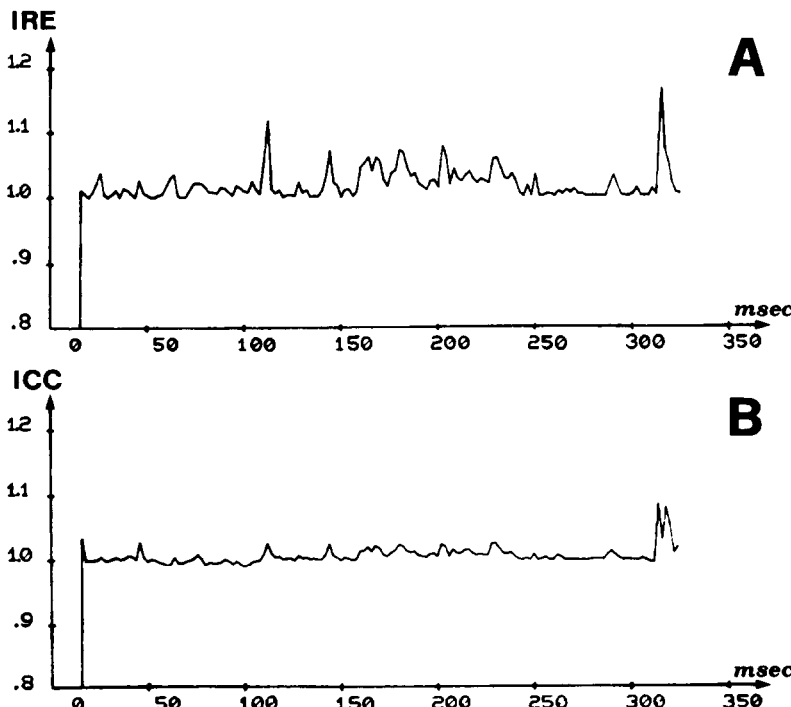


FIG. 16. Time course of the inefficiency indices (a) $\text{IRE}(t)$ and (b) $\text{ICC}(t)$.

We present here a few examples of the results of the inverse procedure (Figures 18–21) related to the P , QRS , and T intervals. The time instants illustrated correspond to those of the simulated surface maps presented in Figs. 7–10. As a general remark, the computed epicardial maps exhibit a sequence of patterns which can be interpreted in terms of electrophysiological intracardiac events, such as epicardial breakthroughs and multiple wave-fronts. It is also worth mentioning that detailed and complex epicardial maps are reconstructed from quite simple body surface patterns.

By applying the inverse numerical procedure to the measured thorax maps at any time instant, we computed the corresponding estimate of the epicardial maps. Since thorax maps, measured at 170 time instants of the heart beat 2 msec apart, were available, we computed an estimate of the time-space potential distribution $u_e(t_j, x_i)$ for $j = 1, \dots, 170$ and $i = 1, \dots, 212$, i.e. for 170 time instants and 212 epicardial locations. As a byproduct, an estimate of the epicardial ECGs was obtained.

We shall now discuss the accuracy of the estimated ECGs from the 212 electrodes on the epicardial frame.

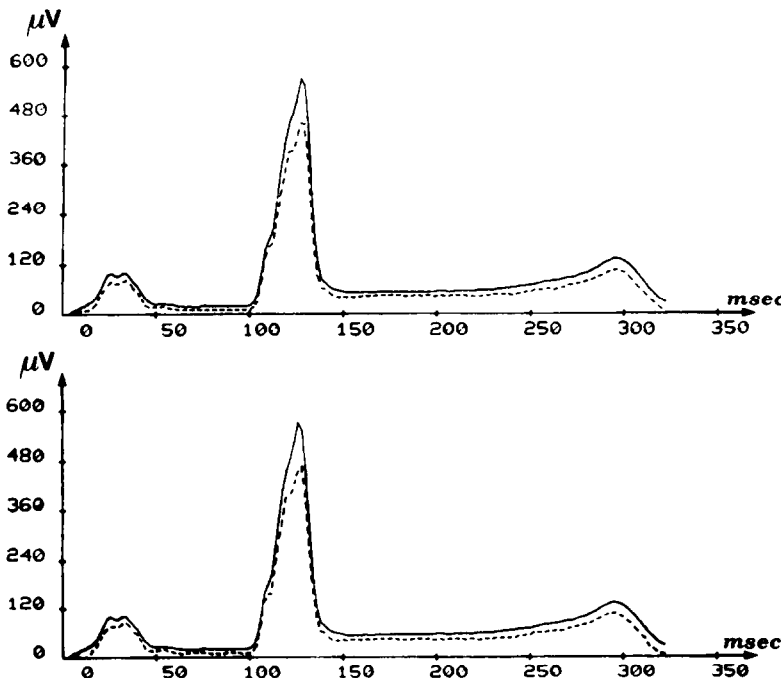


FIG. 17. Comparison between $EEM(t)$ (solid line) and $CEM(t)$ (dashed line) estimated by the optimal (top graph) and by the CRESO (bottom graph) criterion.

In Tables 8, 9 we report the average, over 212 epicardial locations, of some accuracy indices concerning the ECGs obtained using the OPT and CRESO epicardial values. The accuracy was evaluated over different intervals of the heart beat. From these tables we deduce that a good pattern match of the ECGs is obtained globally over the entire heart beat, with a satisfactory accuracy in terms of RE.

An analysis of the anterior and posterior epicardial spatial distribution of the indices $CC(x_i)$ and $RE(x_i)$, $i = 1, \dots, 212$, reported in Tables 10, 11 reveals that the accuracy is not homogeneous over the epicardial frame. The pattern match is better than average, i.e. $CC > 0.9$ and $RE < 0.4$, in a wide area on the anterior and posterior epicardial frame. On the other hand, the accuracy was poor at a few locations (about 12) on the right side of the epicardial frame. Note that the epicardial locations in this region have the largest average distance from the corresponding radially aligned thoracic lead points.

The results on Tables 10 and 11 confirm the excellent performance of the CRESO estimates, analyzed in terms of epicardial ECGs, as compared to the

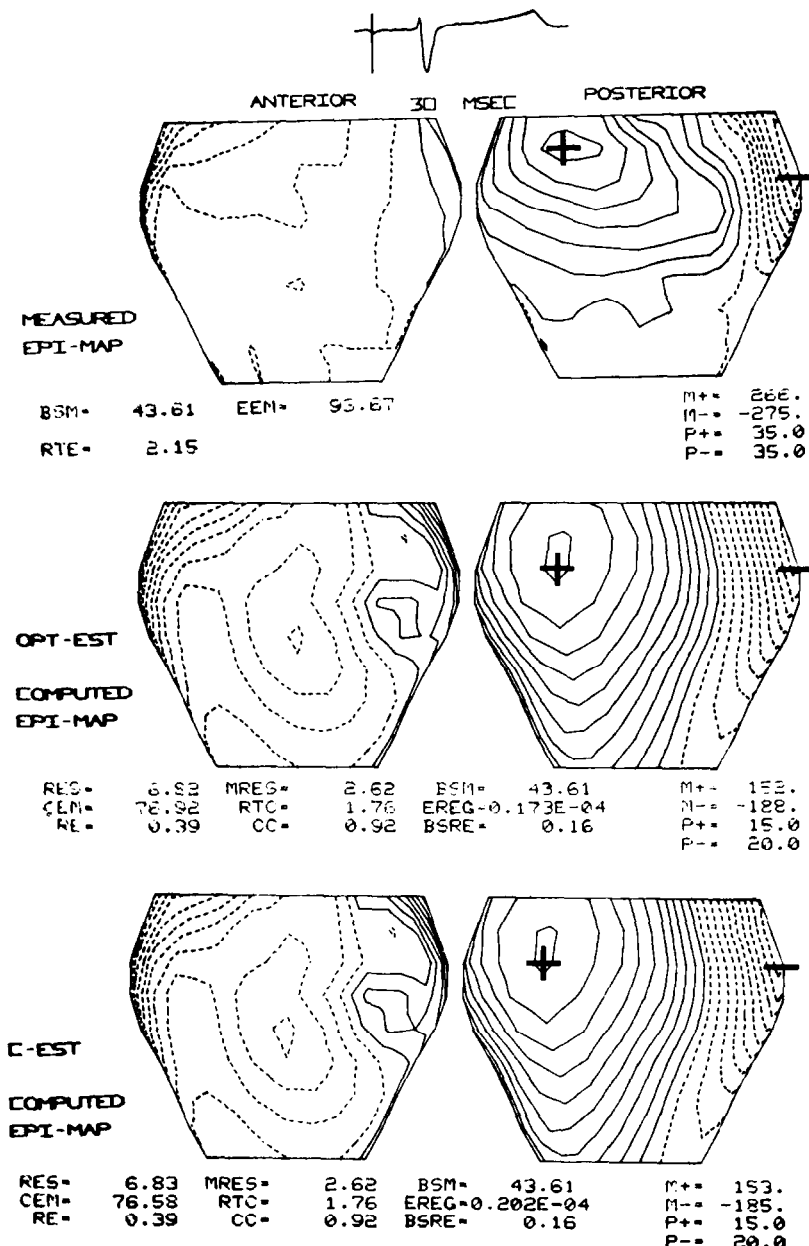


FIG. 18. Measured epicardial maps (top), and optimal (middle) and CRESO (bottom) estimated epicardial maps, at the time instant indicated by a bar on the electrocardiogram, displayed by means of equipotential lines. The estimated maps reported here and in the following Figures 19, 20, 21 were recovered through the inverse procedure from the measured thorax potentials presented in Figure 7-10.

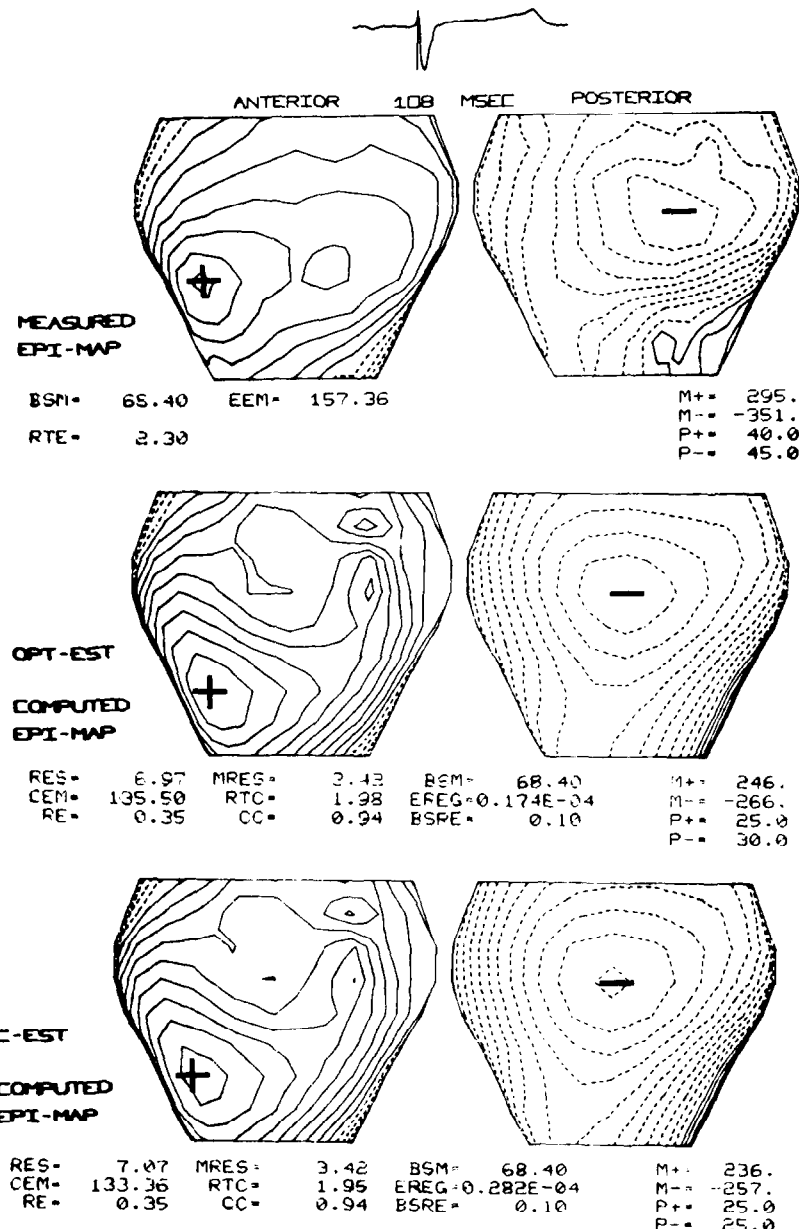


FIG. 19. See Figure 18.

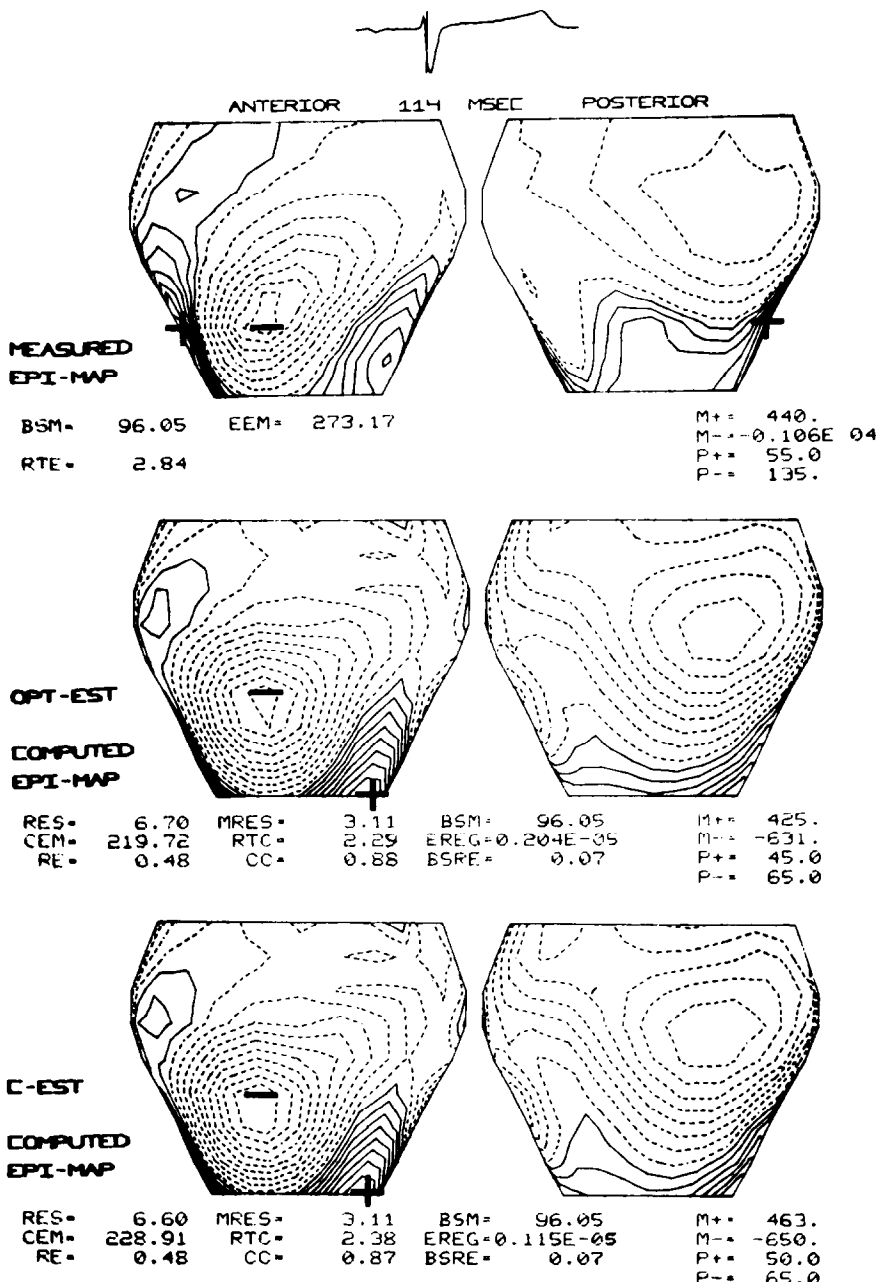


FIG. 20. See Figure 18.

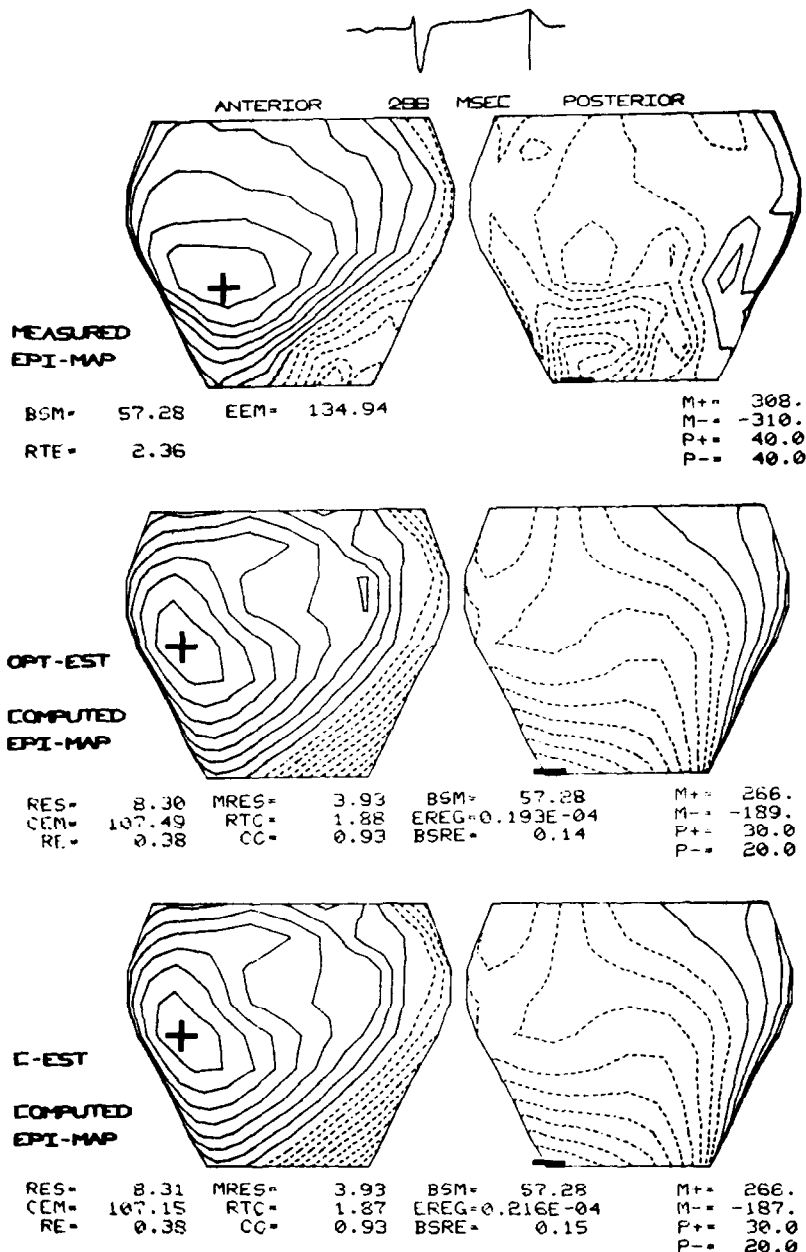


FIG. 21. See Figure 18.

TABLE 8

Inverse Problem: Average Values of Magnitudes and Accuracy Indices
of the Optimal Estimates of the Epicardial ECGs^a

Interval (msec)	Complex	EEM(x)	CEM(x)	RMSE(x)	RE(x)	CC(x)
20–44	P	57.72	52.78	30.17	0.857	0.749
46–102	PQ	19.18	12.65	12.98	0.831	0.611
104–150	QRS	262.60	219.78	113.69	0.494	0.863
152–248	ST	50.75	41.67	27.26	0.841	0.594
248–308	T	83.51	68.19	36.35	0.658	0.827
104–308	QRST	145.57	120.46	63.49	0.464	0.880
20–308	PQRST	126.33	104.16	55.62	0.466	0.889

^a Cardiac electrograms.

OPT estimates. We remark again that the magnitude of the computed epicardial ECGs (cardiac electrograms) is generally underestimated with respect to that of the measured ones, as indicated by the average magnitude reported in Tables 8, 9.

From the high CC between measured and computed ECGs, one may expect that the time of absolute minimum derivative evaluated in the computed (OPT and CRESO) ECGs is a close approximation to the corresponding time instants in the measured ECGs, as evidenced by Figures 22, 23. It is well known that the time of minimum derivative in the epicardial leads corresponds to the passage of the excitation wave under the corresponding electrode. Since our measurements are taken at the same distance from the epicardium, the minimum-derivative times are only an approximation of the excitation times of the underlying epicardium.

TABLE 9

Inverse Problem: Average Values of Magnitudes and Accuracy Indices
of the CRESO Estimates of the Epicardial ECGs^a

Interval (msec)	Complex	EEM(x)	CEM(x)	RMSE(x)	RE(x)	CC(x)
20–44	P	57.72	52.42	30.12	0.842	0.754
46–102	PQ	19.18	11.93	13.05	0.813	0.615
104–150	QRS	262.60	221.53	115.35	0.505	0.859
152–248	ST	50.75	39.76	27.49	0.829	0.642
248–308	T	83.51	68.19	36.57	0.664	0.821
104–308	QRST	145.57	120.97	64.37	0.472	0.876
20–308	PQRST	126.33	104.54	56.38	0.474	0.885

^a Cardiac electrograms.

TABLE 10

Correlation Coefficient $CC(x)$ between Measured and Computed Epicardial ECGs^a

OPT-EST														
	0.97	0.93	0.94	0.90	0.89	0.78	0.95	0.96	0.96	0.95	0.55	0.86	0.92	
A	0.97	0.93	0.94	0.90	0.89	0.78	0.95	0.96	0.96	0.95	0.55	0.86	0.92	
	0.93	0.92	0.	0.90	0.92	0.	0.95	0.79	0.83	0.67	0.90	0.61	0.82	
	0.95	0.89	0.85	0.93	0.91	0.92	0.86	0.95	0.94	0.87	0.72	0.89	0.88	
	0.92	0.60	0.70	0.94	0.97	0.96	0.98	0.96	0.97	0.90	0.94	0.92	0.88	
	0.73	-0.01	0.63	0.93	0.96	0.98	0.99	0.99	0.98	0.97	0.97	0.89	0.82	
	0.52	-0.22	0.72	0.94	0.98	0.99	0.99	0.99	0.99	0.98	0.96	0.93	0.89	
	0.51	0.02	0.84	0.97	0.99	0.99	0.99	0.99	0.97	0.92	0.93	0.95	0.90	
	0.	0.40	0.91	0.	0.99	0.99	0.99	0.96	0.77	0.83	0.84	0.89	0.96	
	0.89	0.87	0.96	0.97	0.98	0.98	0.97	0.94	0.74	0.68	0.87	0.93	0.97	
P	0.92	0.92	0.93	0.85	0.82	0.87	0.87	0.88	0.88	0.85	0.88	0.97	0.97	
	0.82	0.92	0.92	0.91	0.91	0.94	0.96	0.96	0.96	0.94	0.93	0.97	0.93	
	0.88	0.88	0.93	0.94	0.95	0.96	0.95	0.91	0.92	0.96	0.95	0.92	0.95	
	0.88	0.84	0.92	0.95	0.97	0.96	0.97	0.95	0.96	0.97	0.96	0.95	0.92	
	0.82	0.89	0.92	0.95	0.97	0.97	0.96	0.97	0.94	0.97	0.96	0.95	0.73	
	0.89	0.87	0.84	0.88	0.83	0.75	0.75	0.95	0.96	0.98	0.98	0.91	0.52	
	0.90	0.90	0.92	0.88	0.71	0.87	0.94	0.96	0.94	0.92	0.94	0.92	0.51	
	0.96	0.96	0.82	0.92	0.90	0.95	0.97	0.97	0.94	0.96	0.96	0.93	0.	
	0.97	0.83	0.68	0.74	0.84	0.94	0.96	0.97	0.97	0.96	0.93	0.96	0.89	
	C-EST													
A	0.96	0.93	0.94	0.88	0.90	0.77	0.94	0.96	0.97	0.95	0.55	0.84	0.93	
	0.93	0.92	0.	0.87	0.90	0.	0.96	0.78	0.84	0.65	0.92	0.59	0.81	
	0.95	0.87	0.85	0.91	0.89	0.90	0.84	0.96	0.93	0.88	0.73	0.89	0.83	
	0.92	0.57	0.71	0.95	0.96	0.96	0.98	0.96	0.97	0.86	0.95	0.93	0.89	
	0.76	-0.03	0.64	0.94	0.96	0.98	0.99	0.99	0.97	0.96	0.97	0.89	0.81	
	0.56	-0.22	0.72	0.93	0.97	0.99	0.99	0.99	0.99	0.98	0.96	0.93	0.88	
	0.57	-0.00	0.84	0.96	0.99	0.99	0.99	0.99	0.97	0.92	0.92	0.94	0.88	
	0.	0.38	0.90	0.	0.99	0.99	0.99	0.95	0.75	0.85	0.85	0.89	0.95	
	0.88	0.87	0.96	0.97	0.99	0.98	0.97	0.94	0.74	0.67	0.67	0.93	0.97	
P	0.93	0.91	0.94	0.85	0.79	0.80	0.86	0.87	0.86	0.83	0.87	0.97	0.96	
	0.81	0.91	0.93	0.91	0.89	0.93	0.96	0.95	0.95	0.93	0.94	0.98	0.93	
	0.83	0.86	0.92	0.94	0.96	0.97	0.95	0.91	0.92	0.96	0.94	0.92	0.95	
	0.89	0.81	0.90	0.94	0.97	0.97	0.98	0.94	0.95	0.97	0.95	0.94	0.92	
	0.81	0.88	0.91	0.94	0.97	0.97	0.96	0.96	0.94	0.97	0.96	0.95	0.76	
	0.88	0.84	0.81	0.88	0.83	0.74	0.75	0.94	0.96	0.98	0.98	0.91	0.56	
	0.88	0.86	0.89	0.88	0.70	0.86	0.94	0.96	0.94	0.92	0.94	0.93	0.57	
	0.95	0.96	0.83	0.92	0.89	0.95	0.97	0.97	0.94	0.96	0.96	0.93	0.	
	0.97	0.84	0.69	0.75	0.85	0.94	0.96	0.97	0.97	0.95	0.92	0.96	0.88	

^aOPT and CRESO, over the entire heart beat, are reported on the anterior (A) and posterior (P) epicardial frame. The values are ordered from top as the 9 rows of 24 electrodes on the cage. The first column in A (right side of the heart) is repeated as last column in P, and vice versa. The 4 zero values indicate leads with poor electric contact. The figures are rounded off to two decimals.

TABLE 11

Relative Error $RE(x)$ between Measured and Computed Epicardial ECGs^a

OPT-EST														
A	0.31	0.40	0.42	0.47	0.54	0.59	0.30	0.35	0.47	0.35	0.87	0.61	0.55	
	0.43	0.43	0.	0.40	0.34	0.	0.24	0.52	0.47	0.90	0.70	1.06	0.53	
	0.43	0.50	0.49	0.31	0.35	0.27	0.42	0.42	0.41	0.50	0.80	0.90	0.56	
	0.47	0.87	0.87	0.38	0.26	0.28	0.37	0.52	0.42	0.54	0.50	0.61	0.54	
	0.72	1.26	1.04	0.48	0.30	0.27	0.29	0.35	0.34	0.31	0.32	0.54	0.59	
	0.85	1.17	0.79	0.39	0.27	0.18	0.27	0.34	0.35	0.28	0.34	0.47	0.52	
	0.83	1.01	0.55	0.29	0.24	0.31	0.35	0.38	0.31	0.39	0.40	0.43	0.54	
	0.	0.89	0.45	0.	0.23	0.28	0.34	0.45	0.77	0.57	0.55	0.47	0.31	
	0.44	0.45	0.29	0.35	0.23	0.31	0.36	0.56	0.85	0.86	0.64	0.49	0.39	
P	0.55	0.39	0.29	0.39	0.50	0.43	0.42	0.44	0.46	0.51	0.47	0.34	0.31	
	0.53	0.36	0.45	0.35	0.77	0.38	0.29	0.30	0.29	0.50	0.37	0.34	0.43	
	0.56	0.48	0.35	0.39	0.29	0.28	0.30	0.39	0.37	0.31	0.37	0.49	0.43	
	0.54	0.54	0.40	0.31	0.27	0.29	0.28	0.34	0.31	0.23	0.34	0.41	0.47	
	0.59	0.48	0.39	0.39	0.31	0.32	0.40	0.31	0.44	0.34	0.35	0.44	0.72	
	0.52	0.59	0.58	0.57	0.57	0.71	0.75	0.37	0.44	0.35	0.37	0.55	0.85	
	0.54	0.46	0.47	0.53	0.74	0.56	0.37	0.48	0.39	0.44	0.37	0.57	0.83	
	0.31	0.36	0.60	0.40	0.63	0.49	0.46	0.34	0.53	0.27	0.32	0.41	0.	
	0.39	0.58	0.77	0.71	0.69	0.39	0.32	0.42	0.51	0.61	0.69	0.36	0.44	
C-EST														
A	0.33	0.40	0.41	0.48	0.53	0.61	0.33	0.36	0.46	0.32	0.89	0.64	0.53	
	0.45	0.45	0.	0.46	0.38	0.	0.23	0.53	0.47	0.85	0.67	1.09	0.59	
	0.47	0.56	0.49	0.35	0.38	0.30	0.44	0.39	0.42	0.47	0.79	0.86	0.65	
	0.50	0.91	0.89	0.35	0.27	0.30	0.36	0.54	0.43	0.59	0.50	0.57	0.55	
	0.70	1.27	1.06	0.50	0.31	0.27	0.29	0.36	0.33	0.31	0.31	0.53	0.59	
	0.84	1.17	0.82	0.43	0.30	0.19	0.28	0.35	0.34	0.25	0.34	0.47	0.54	
	0.82	1.03	0.58	0.31	0.24	0.30	0.35	0.39	0.33	0.41	0.43	0.46	0.58	
	0.	0.92	0.47	0.	0.21	0.26	0.34	0.47	0.80	0.56	0.54	0.47	0.34	
	0.46	0.46	0.30	0.32	0.21	0.29	0.36	0.58	0.88	0.88	0.66	0.52	0.42	
P	0.53	0.44	0.28	0.40	0.52	0.45	0.43	0.45	0.49	0.51	0.47	0.35	0.33	
	0.59	0.35	0.43	0.34	0.75	0.38	0.29	0.30	0.31	0.48	0.35	0.35	0.45	
	0.65	0.47	0.35	0.38	0.28	0.25	0.31	0.39	0.37	0.31	0.38	0.51	0.47	
	0.55	0.57	0.44	0.33	0.26	0.25	0.26	0.35	0.33	0.24	0.36	0.43	0.50	
	0.59	0.49	0.40	0.37	0.30	0.30	0.39	0.32	0.45	0.34	0.35	0.43	0.70	
	0.54	0.63	0.62	0.55	0.56	0.72	0.76	0.38	0.45	0.35	0.37	0.54	0.84	
	0.58	0.51	0.52	0.53	0.74	0.58	0.38	0.48	0.39	0.44	0.38	0.56	0.82	
	0.34	0.37	0.58	0.39	0.63	0.49	0.45	0.33	0.55	0.28	0.34	0.42	0.	
	0.42	0.58	0.77	0.71	0.69	0.39	0.33	0.45	0.54	0.65	0.73	0.39	0.46	

^aOPT and CRESO, over the entire heart beat, displayed as in Table 10.

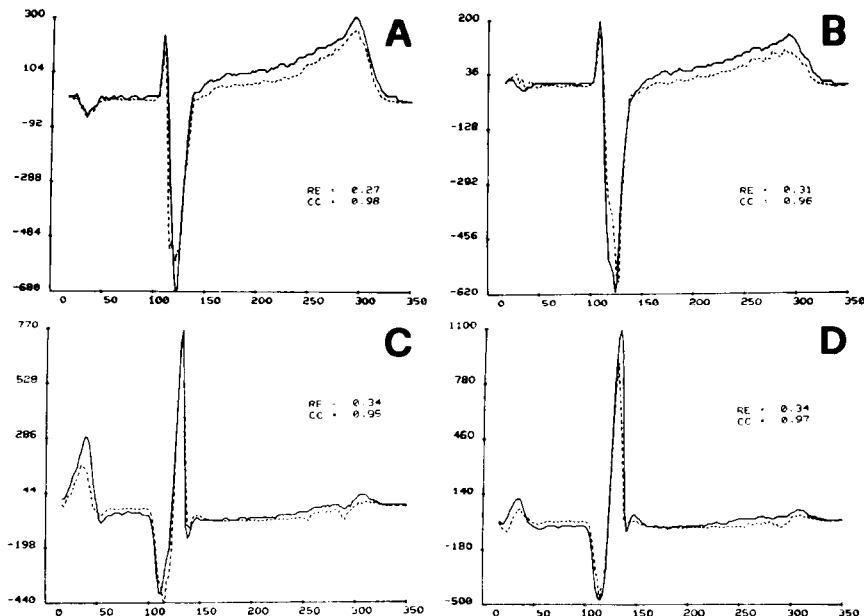


FIG. 22. Comparison between measured (solid line) and computed (dashed line) ECGs at four different lead locations on the epicardium: right (a) and left (b) anterior sites; central (c) and right (d) posterior sites. The computed ECGs were obtained using the optimal epicardial estimates over the entire heart beat.

DISCUSSION AND CONCLUSIONS

We have shown how, in an experiment *in vitro* with realistic distances of the epicardial frame from the thorax-shaped tank, it is possible to recover the potential distributions on the epicardial frame with good quality in terms of pattern match and with a quantitative accuracy expressed by a relative error less than 0.5 in the *QRS* and *T* waves. Taking into account the present-day quantitative and qualitative criteria for interpreting epicardial maps, it seems that the computed epicardial maps yield a great portion of the information contained in the measured ones. This positive result is enhanced if one considers the computed epicardial ECGs, which exhibit a relative error of less than 0.4 over large portions of the anterior and posterior epicardial frame.

Comparing the results of this experiment with those of a previous one reported in [8], we remark that better and more uniform accuracy of the reconstructed epicardial maps has been achieved, as measured by an average increase of 10 percent in the cc. This might be attributed chiefly to the more realistic geometry, with the heart placed near the anterior thorax surface,

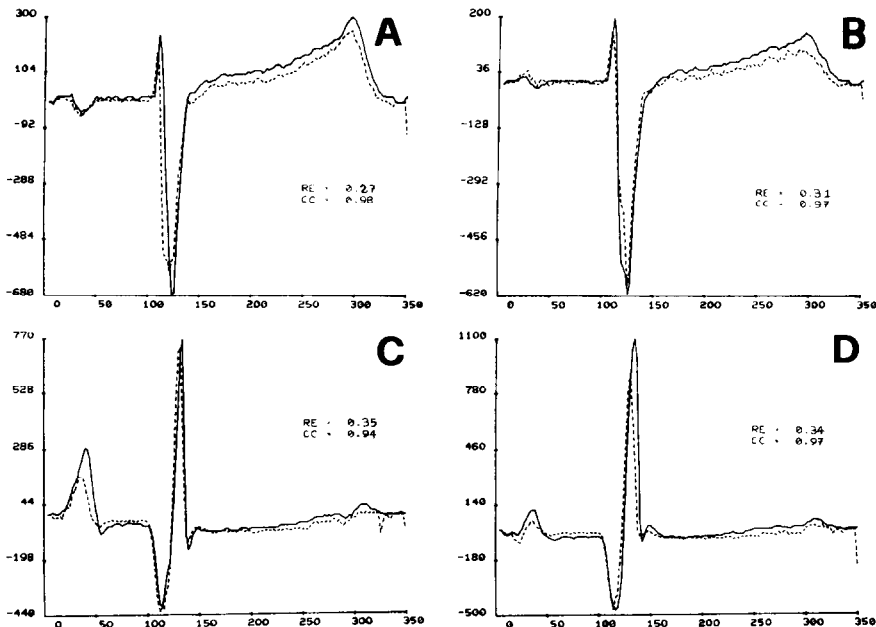


FIG. 23. The same four measured epicardial ECGs (solid lines) reported in Figure 22 are compared with the computed ECGs (dashed line) obtained by using the CRESO estimates over the entire heart beat.

whereas in the previous experiment the heart was located in a central position inside a cylindrical tank.

In the present experiment it was possible to obtain epicardial maps with an accuracy measured by an RE lower than 0.4 over parts of the *P*, *QRS*, and *T* intervals. This good accuracy was achieved in those time intervals where the simulated-thorax data, related to the direct problem, exhibited an RE less than 0.3.

We believe that this higher level of accuracy of the computed epicardial maps with an RE of 0.3–0.4 could be extended to the entire heart beat if the overall noise level on the data were significantly reduced, as suggested by the results obtained in applying the inverse procedure to test functions. In our opinion this goal may be reached through:

- (1) An improvement of the data quality obtained by averaging over several beats, which is essential for achieving a good recovery of the potential patterns in the *PQ* interval, where the signal magnitude is particularly low.
- (2) A reduction of the time-alignment errors, which become sizable in the *QRS* complex, where rapid changes of the signals occur. This reduction could

be obtained by means of a higher frequency of sampling and a more accurate time interpolation of the data, thus leading to a better synchronization of the experimental maps. This should allow one to obtain estimates of the epicardial potentials having a more uniform and higher accuracy in the *QRS* interval.

In the present experiment *in vitro*, the conductivity of the physiological solution was higher than the average conductivity of the human torso; this led to recording of thorax data with a lower magnitude and *S/N* ratio than those usually collected in human subjects.

Actually in the *in vitro* experiment the peak magnitudes of the thorax maps in the *P*, *QRS*, and *T* intervals were about 50, 150, and 60 μV , whereas generally in human subjects the corresponding values are about 50, 1000, and 300 μV or more. Therefore in the *in vitro* experimental situation it is necessary to have better accuracy in the measured data in order to achieve a *S/N* ratio comparable to that obtainable in human subjects.

A further problem, besides the accuracy assessment just pointed out, is that of establishing which body inhomogeneities, if any [3], should be taken into account to obtain meaningful estimates of the epicardial potential from *in vivo* data (for some model studies see [21, 13]).

Concerning the choice of the regularization parameter, the formulation and the performance evaluation of the CRESO criterion seems of great interest for the application of the inverse procedure as a noninvasive technique, i.e. for the prediction of the epicardial potential distributions when only body surface potentials are available. We recall that CRESO utilizes only thorax potential measurements without any knowledge of the noise affecting them, and that its efficiency was demonstrated by the good match between the computed and the measured epicardial patterns as well as by the close agreement with the epicardial optimal estimates (OPT-EST).

The analysis of the computed epicardial ECGs (cardiac electrograms) indicates that the waveforms are very well reproduced; hence these ECGs could be used for determining the epicardial excitation sequence, which is of great significance in the study of the bioelectrical activity of the heart.

REFERENCES

- 1 A. C. L. Barnard, J. M. Duck, and M. S. Lynn, The application of electromagnetic theory to electrocardiology I: Derivation of the integral equation, *Biophys. J.* 7:443–462 (1967).
- 2 R. C. Barr, M. Ramsey III, and M. S. Spach, Relating epicardial to body surface potential distributions by means of transfer coefficients based on geometry measurements, *IEEE Trans. Biomed. Engrg.* BME-24:1–11 (1977).
- 3 R. C. Barr and M. S. Spach, Inverse calculation of *QRS-T* epicardial potentials from body surface potential distributions for normal and ectopic beats in the intact dog, *Circ. Res.* 42:661–675 (1978).

- 4 P. Colli Franzone, Regularization methods applied to an inverse problem in electrocardiology, in *Computing Methods in Applied Sciences and Engineering* (R. Glowinski and J. L. Lions, Eds.), North Holland, 1980, pp. 615–633.
- 5 P. Colli Franzone and E. Magenes, On the inverse potential problem of electrocardiology, *Calcolo* 16:459–538 (1979).
- 6 P. Colli Franzone, B. Taccardi, and C. Viganotti, An approach to inverse calculation of epicardial potentials from body surface maps, *Adv. Cardiology (Karger, Basel)* 21:167–170 (1977).
- 7 P. Colli Franzone, L. Guerri, and C. Viganotti, Relating surface to epicardial potentials with direct and inverse calculations, in *Simulations of Systems*, North Holland, New York, 1979, pp. 665–674.
- 8 P. Colli Franzone, L. Guerri, B. Taccardi, and C. Viganotti, The direct and inverse potential problem in electrocardiology. Numerical aspects of some regularization methods and application to data collected in isolated dog heart experiments, Publ. No. 222, IAN-CNR, Pavia, 1979, pp. 1–82.
- 9 P. Colli Franzone, L. Guerri, B. Taccardi, and C. Viganotti, Numerical procedure to inversely compute epicardial potentials from body surface maps applied to a normal human subject, in *Computers in Cardiology*, IEEE Computer Soc. Press, 1982, pp. 187–190.
- 10 P. Colli Franzone, L. Guerri, B. Taccardi, and C. Viganotti, The inverse potential problem applied to the human case, in *Models and Measurements of Cardiac Electric Fields* (E. Schubert, Ed.), Plenum, New York, 1982, pp. 19–33.
- 11 P. Colli Franzone, L. Guerri, B. Taccardi, and C. Viganotti, Finite element approximation of regularized solutions of the inverse potential problem of electrocardiography applied to canine and human data, *Calcolo*, to appear.
- 12 C. Cottini, D. Dotti, E. Gatti, and B. Taccardi, A 240-probe instrument for mapping cardiac potentials, in *The Electric Field of the Heart* (P. Rijlant, Ed.), Presses Académiques Européennes, Bruxelles, 1972, pp. 99–102.
- 13 R. M. Gubrajani and G. E. Mailloux, A simulation study of the effects of torso inhomogeneities on electrocardiographic potentials, using realistic heart and torso models, *Circ. Res.* 52:45–56 (1983).
- 14 B. M. Irons, A frontal solution program for finite element analysis, *Internat. J. Numer. Methods Engrg.* 2:5–32 (1970).
- 15 M. A. Jaswon and G. T. Symm, *Integral Equation Methods in Potential Theory and Elastostatics*, Academic, London, 1977.
- 16 R. O. Martin, T. C. Pilkington, and M. N. Morrow, Statistically constrained inverse electrocardiography, *IEEE Trans. Biomed. Engrg.* BME-22:487–492 (1975).
- 17 T. C. Pilkington and R. Plonsey (Eds.), *Engineering Contributions to Biophysical Electrocardiography*, IEEE Press, 1982, Chapter 9.
- 18 R. Plonsey and D. G. Fleming, *Bioelectric Phenomena*, McGraw-Hill, New York, 1969.
- 19 R. Plonsey and D. Heppner, Considerations of quasistationarity in electrophysiological systems, *Bull. Math. Biophys.* 29:657–664 (1967).
- 20 M. Ramsey III, R. C. Barr, and M. S. Spach, Comparison of measured torso potentials with those simulated from epicardial potentials for ventricular depolarization and repolarization in the intact dog, *Circ. Res.*, 41:660–672 (1977).
- 21 Y. Rudy and R. Plonsey, A comparison of volume conductor and source geometry effects on body surface and epicardial potentials, *Circ. Res.* 46:283–291 (1980).
- 22 G. Strang and G. J. Fix, *An Analysis of the Finite Element Method*, Prentice-Hall, Englewood Cliffs, N.J., 1973.

- 23 A. H. Stroud, Some fifth degree integration formulas for symmetric regions, *Math. Comp.* 20:90–97 (1966).
- 24 B. Taccardi, Distribution of heart potential on the thoracic surface of normal human subjects, *Circ. Res.* 12:341–352 (1963).
- 25 B. Taccardi, E. Musso, and L. De Ambroggi, Current and potential distribution around an isolated dog heart, in *The Electrical Field of the Heart* (P. Rijlant, Ed.), Presses Académiques Européennes, Bruxelles, 1972, pp. 566–572.
- 26 B. Taccardi, C. Viganotti, E. Macchi, and L. De Ambroggi, Relationships between the current field surrounding an isolated dog heart and the potential distribution on the surface of the body, *Adv. Cardiol. (Karger, Basel)* 16:72–76 (1976).
- 27 A. N. Tikhonov and V. J. Arsenin, *Solution of Ill-Posed Problems*, Wiley, New York, 1977.
- 28 C. Van Loan, Generalizing the singular value decomposition, Technical Report No. 7, Univ. of Manchester, 1974.
- 29 C. Van Loan, Generalizing the singular value decomposition, *SIAM J. Numer. Anal.* 13:76–83 (1976).
- 30 M. M. Varah, A practical examination of some numerical methods for linear discrete ill-posed problems, *SIAM Rev.* 21:100–111 (1979).
- 31 Y. Yamashita, Inverse solution in electrocardiography, *Japan Circ. J.* 45:1312–1322 (1982).
- 32 C. Zienkiewicz, *The Finite Element Method in Engineering Science*, McGraw-Hill, London, 1971.